The Astrophysical Journal, 732:126 (17pp), 2011 May 10 doi:10.1088/0004-637X/732/2/126

AN ACCOUNTING OF THE DUST-OBSCURED STAR FORMATION AND ACCRETION HISTORIES OVER THE LAST ∼11 BILLION YEARS

E. J. Murphy[1], R.-R. Chary[1], M. Dickinson[2], A. Pope[2,3,6], D. T. Frayer[4], and L. Lin[5]
[1] Spitzer Science Center, MC 314-6, California Institute of Technology, Pasadena, CA 91125, USA; emurphy@ipac.caltech.edu
[2] National Optical Astronomy Observatory, Tucson, AZ 85719, USA
[3] Department of Astronomy, University of Massachusetts, Amherst, MA 01003, USA
[4] National Radio Astronomy Observatory, P.O. Box 2, Green Bank, WV 24944, USA
[5] Institute of Astronomy & Astrophysics, Academia Sinica, Taipei 106, Taiwan
Received 2010 September 13; accepted 2011 February 18; published 2011 April 26

ABSTRACT

We report on an accounting of the star-formation- and accretion-driven energetics of 24 μm-detected sources in the Great Observatories Origins Deep Survey-North field. For sources having infrared (IR; 8–1000 μm) luminosities $\gtrsim 3 \times 10^{12}\,L_{\odot}$ when derived by fitting local spectral energy distributions (SEDs) to 24 μm photometry alone, we find these IR luminosity estimates to be a factor of ∼4 times larger than those estimated when the SED fitting includes additional 16 and 70 μm data (and in some cases mid-IR spectroscopy and 850 μm data). This discrepancy arises from the fact that high-luminosity sources at $z \gg 0$ appear to have far- to mid-IR ratios, as well as aromatic feature equivalent widths, typical of lower luminosity galaxies in the local universe. Using our improved estimates for IR luminosity and active galactic nucleus (AGN) contributions, we investigate the evolution of the IR luminosity density versus redshift arising from star formation and AGN processes alone. We find that, within the uncertainties, the total star-formation-driven IR luminosity density is constant between $1.15 \lesssim z \lesssim 2.35$, although our results suggest a slightly larger value at $z \gtrsim 2$. AGNs appear to account for $\lesssim$18% of the total IR luminosity density integrated between $0 \lesssim z \lesssim 2.35$, contributing $\lesssim$25% at each epoch. Luminous infrared galaxies (LIRGs; $10^{11}\,L_{\odot} \leqslant L_{\rm IR} < 10^{12}\,L_{\odot}$) appear to dominate the star formation rate density along with normal star-forming galaxies ($L_{\rm IR} < 10^{11}\,L_{\odot}$) between $0.6 \lesssim z \lesssim 1.15$. Once beyond $z \gtrsim 2$, the contribution from ultraluminous infrared galaxies ($L_{\rm IR} \geqslant 10^{12}\,L_{\odot}$) becomes comparable with that of LIRGs. Using our improved IR luminosity estimates, we find existing calibrations for UV extinction corrections based on measurements of the UV spectral slope typically overcorrect UV luminosities by a factor of ∼2, on average, for our sample of 24 μm-selected sources; accordingly we have derived a new UV extinction correction more appropriate for our sample.

Key words: galaxies: evolution – infrared: galaxies – radio continuum: galaxies – ultraviolet: galaxies

Online-only material: color figures

1. INTRODUCTION

Precisely quantifying the stellar mass assembly over cosmic time is critical for understanding galaxy formation and evolution. While the first studies which set out to characterize the cosmic star formation history had to rely on observations of the emergent (rest-frame) UV emission, requiring significant corrections for extinction by dust, the advent of space-based infrared (IR) observatories have allowed us to measure the dust-obscured star formation activity directly. The resolution of the cosmic infrared background using the *Infrared Space Observatory* (*ISO*; e.g., Elbaz et al. 2002), *Spitzer* (e.g., Dole et al. 2006), and now *Herschel* (e.g., Berta et al. 2010), has uncovered populations of dusty, starbursting galaxies with infrared (8–1000 μm) luminosities ranging between $10^{10}\,L_{\odot} \lesssim L_{\rm IR} \lesssim 10^{13}\,L_{\odot}$. These cosmologically important luminous ($10^{11}\,L_{\odot} \leqslant L_{\rm IR} < 10^{12}\,L_{\odot}$) and ultraluminous ($L_{\rm IR} \geqslant 10^{12}\,L_{\odot}$) infrared galaxies, LIRGs and ULIRGs, respectively, appear to dominate the star formation rate (SFR) density in the universe between redshifts of $1 \lesssim z \lesssim 3$ (e.g., Chary & Elbaz 2001; Le Floc'h et al. 2005; Caputi et al. 2007).

Many of these studies rely on deep 24 μm imaging and the use of local spectral energy distribution (SED) libraries to extrapolate the evolution of the total infrared luminosity with redshift. In doing so, large (factors of ∼10) bolometric corrections are invoked to scale up the rest-frame mid-infrared flux densities and estimate the total SFR per unit co-moving volume. Using the rest-frame mid-infrared wavelengths, specifically near ∼8 μm, can be problematic due to the presence of broad spectral features attributed to polycyclic aromatic hydrocarbon (PAH) molecules. While the rest-frame 8 μm emission correlates with the total IR luminosity of galaxies in the local universe, albeit with a large amount of scatter (e.g., Dale et al. 2005; Smith et al. 2007; Armus et al. 2007) and systematic departures for low-metallicity systems (e.g., Engelbracht et al. 2006; Madden et al. 2006), there are hints that this correlation may break down at increasing redshift. In a recent study, Murphy et al. (2009) have shown that galaxies in the redshift range between $1.4 \lesssim z \lesssim 2.6$ exhibit PAH equivalent widths that are large compared to local galaxies of similar luminosity. This translates into an overestimate of IR luminosities from rest-frame mid-infrared photometry which has been noted for subsets of $z \sim 2$ galaxies (e.g., Papovich et al. 2007; Rigby et al. 2008; Elbaz et al. 2010; Nordon et al. 2010).

An additional uncertainty arises from the fact that a fraction of the light emitted by these IR-bright galaxies may also be associated with embedded active galactic nuclei (AGNs). The separation of the AGN and star-forming component of a galaxy's IR output requires knowledge of its full SED, which is difficult to measure for a large number of high-redshift systems. One technique to get at this separation of AGN and star formation

[6] Spitzer Fellow.

Table 1
Number of Detections within ACS Coverage

16 μm	24 μm	70 μm	Optical (z_{850})	Hard X-ray
1122	2196	133	1884	156

Note. Out of a total of 2664 24 μm-detected sources.

activity is through the use of mid-infrared spectroscopy where one decomposes the spectra into aromatic feature and continuum components (e.g., Sajina et al. 2007; Pope et al. 2008; Murphy et al. 2009). For a heterogenous sample of IR-bright galaxies, this technique has revealed that the contribution of AGN to the total IR luminosity output can span a large range, and is, on average, non-negligible being roughly ∼30% (Murphy et al. 2009).

In this paper, we use deep 70 μm data from the Far-Infrared Extragalactic Deep Legacy (FIDEL; PI: M. Dickinson) survey to provide improved estimates for the total IR luminosities of 24 μm-selected sources in the Great Origins Observatories Deep Survey-North (GOODS-N; Dickinson et al. 2003) field out to $z \approx 2.8$. Using these improved values, along with an empirical relation for the fractional AGN contribution to the total IR luminosities of the 24 μm-selected sources, we show how the IR luminosity density evolves separately for AGN and star formation versus redshift. In doing so, we also look at how the contribution from populations of normal galaxies ($L_{\rm IR} < 10^{11}\ L_{\odot}$), LIRGs, and ULIRGs to the SFR density varies as a function of lookback time.

The paper is organized as follows. In Section 2, we describe the sample properties and observations. IR luminosity estimates through SED fitting, along with a description of how we estimate contributions from AGN, are discussed in Section 3. A look into the applicability of standard UV extinction estimates from the UV spectral slope for our sample of 24 μm-selected sources is given in Section 4. A discussion of the results on the evolution of the IR luminosity density versus redshift is given in Section 5, along with an explicit description of the uniqueness of this study. Finally, in Section 6, we summarize our conclusions.

2. SAMPLE SELECTION AND MULTIWAVELENGTH PHOTOMETRY

The GOODS-N field is located around the Hubble Deep Field-North at $12^{\rm h}36^{\rm m}55^{\rm s}$, $+62^{\circ}14'15''$ (J2000). In Figure 1, we overlay source detections on the 70 μm image of GOODS-N (Frayer et al. 2006) and provide a summary of the source detections at 16, 24, and 70 μm, as well as in the optical and hard-band (2.0–8.0 keV) X-rays in Table 1 (see Appendix A for details of existing radio data). The total number of sources detected in all three infrared bands is 112. The multiwavelength data used here are the same that were used in the analysis of the mid-infrared spectroscopic sample presented in Murphy et al. (2009).

2.1. Mid- and Far-infrared Spitzer Imaging

Spitzer observations at 16, 24, and 70 μm of the GOODS-N field were taken as part of various programs. Observations at 24 μm using the Multiband Imaging Photometer for *Spitzer* (MIPS; Rieke et al. 2004) were taken as part of the GOODS Legacy program (PI: M. Dickinson) and reach an rms of ∼5 μJy (see Chary 2007). The catalog was created using IRAC prior positions and sources having a 24 μm flux density greater than 20 μJy and a signal-to-noise ratio (S/N) greater than 3 were considered to be detections leading to a total number of 2664 detections; a 24 μm flux density of 30 μJy corresponds to a differential completeness of ≈80% (Magnelli et al. 2009). The 24 μm flux density among these sources spans a range between ∼20 and 4320 μJy, more than a factor of ∼200; the median flux density is ∼70 μJy. Calibration uncertainty at 24 μm is ∼10%.

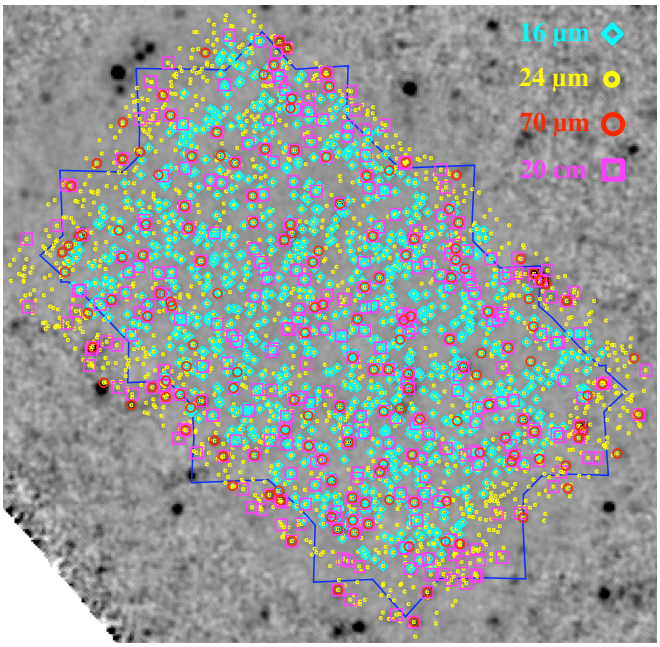

Figure 1. Location for each of the 2664 24 μm-detected sources overlaid on the MIPS 70 μm map of the GOODS-N field. Corresponding detections at 16 μm, 70 μm, and 20 cm are shown; note that the areal coverage of the 16 μm map is smaller than the extent of the 24 μm observations. The blue outline shows the ≈160 arcmin^2 ACS areal coverage over which our analysis of the IR luminosity evolution vs. redshift is conducted.

(A color version of this figure is available in the online journal.)

Of the 2664 24 μm detections a total of 2196 sources are included within the optical (*Hubble* Advanced Camera for Surveys (ACS); see Section 2.3) areal coverage of the GOODS-N field with 1111 spectroscopic redshifts available (Cohen et al. 2000; Wirth et al. 2004; Barger et al. 2008; D. Stern et al. 2011, in preparation). The differential spectroscopic completeness as a function of the 24 μm flux density is plotted in Figure 2, along with the corresponding 24 μm number counts. Among these sources having spectroscopic redshifts, 1105 are at $z < 3$ having a median value of ≈0.845 (see Table 2 for a breakdown using six redshift bins). The 24 μm flux densities of these sources span a range from ∼20 to 2440 μJy (i.e., a factor of ∼120), with a median value of ∼80 μJy

Imaging at 16 μm was carried out using one of the two peak-up array cameras for the Infrared Spectrograph for *Spitzer* (IRS; Houck et al. 2004). Details of the imaging program and catalog can be found in Teplitz et al. (2005, 2011). The areal coverage of the 16 μm map was slightly smaller than that of the GOODS-N 24 μm map (see Figure 1). The rms noise of these data is ∼6 μJy and only sources having S/Ns greater than 5 were considered to be firm detections leading to a total of 1297 sources detected. Of these, 1154 have 24 μm counterparts (1122 within the ACS coverage), while 775 of these also had spectroscopic redshifts; 769 were at $z < 3$. Among these 769 sources, their 16 μm flux densities span a range from ∼30 to 1420 μJy (i.e., a factor of nearly ∼50) with a median value of 95 μJy. The calibration uncertainly at 16 μm is ∼10% and all non-detections were assigned the upper limit value of 30 μJy.

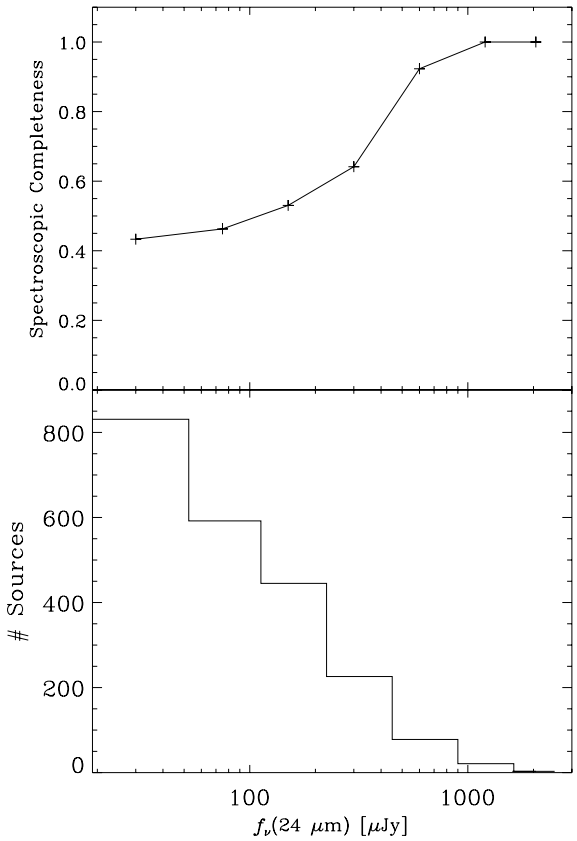

Figure 2. In the top panel, the spectroscopic completeness for the 24 μm sources included in the areal coverage of the ACS imaging is plotted against the 24 μm flux density. The completeness is differential, illustrating the fraction of sources with spectroscopic redshifts per each 24 μm flux density bin. The bottom panel shows total number counts of 24 μm sources per flux density bin.

Deep MIPS 70 μm observations centered on, and extending beyond, the GOODS-N field were performed as part of two separate imaging programs; GO-3325 (PI: D. T. Frayer; Frayer et al. 2006) and the FIDEL project (PI: M. Dickinson). The typical point-source noise of the 70 μm map is ~0.55 mJy (Frayer et al. 2006) which is roughly ~1.6 times larger than the confusion noise level of $\sigma_c = 0.35 \pm 0.15$ mJy (Frayer et al. 2009). Details of the data processing can be found in Frayer et al. (2006). The cataloged sources were considered detections if their 70 μm flux density was >2 mJy and they had an S/N > 6; these criteria correspond to a differential completeness of ~80% (Magnelli et al. 2009) and a total of 167 sources are detected, 164 of which had 24 μm counterparts (133 within the ACS coverage). Of the 164 sources matched with a 24 μm counterpart, 123 also had spectroscopic redshifts, all of which were at $z < 3$. The 70 μm flux densities range between ~2 and 19 mJy, spanning nearly an order of magnitude, and have a median value of 3.7 mJy. Sources not meeting the detection criteria were assigned the upper limit value of 3 mJy. The calibration uncertainty at 70 μm is ~20%. A summary of the total number source detections at 16, 24, and 70 μm within the ACS areal coverage can be found in Table 1.

2.2. X-ray Imaging

GOODS-N was observed using the *Chandra X-ray Observatory* for a 2 Ms exposure (Alexander et al. 2003). The full band (0.5–8.0 keV) and hard band (2.0–8.0 keV) on-axis sensitivities are $\sim 7.1 \times 10^{-17}$ and 1.4×10^{-16} erg cm^{-2} s^{-1}, respectively. Of the 2196 24 μm-detected sources included in the ACS areal coverage, 223 were matched with an X-ray counterpart reported by Alexander et al. (2003). A total of 156 of these sources have firm detections in the hard band.

Table 2
Sources per z Bin

Redshift	$N_{24\,\mu\mathrm{m}}$	$N_{70\,\mu\mathrm{m}}$
Spectroscopic redshifts		
$0.0 \leqslant z < 0.4$	111	30
$0.4 \leqslant z < 0.7$	310	43
$0.7 \leqslant z < 1.0$	338	28
$1.0 \leqslant z < 1.3$	176	12
$1.3 \leqslant z < 1.9$	90	6
$1.9 \leqslant z < 2.8$	76	3
Spectroscopic and photometric redshifts		
$0.0 \leqslant z < 0.4$	123	31
$0.4 \leqslant z < 0.7$	333	43
$0.7 \leqslant z < 1.0$	430	28
$1.0 \leqslant z < 1.3$	333	15
$1.3 \leqslant z < 1.9$	349	6
$1.9 \leqslant z < 2.8$	362	4

Note. Only sources within the ACS areal coverage are considered. There are two sources with spectroscopic redshifts outside of the ACS areal coverage, as well as four additional sources with spectroscopic redshifts between $2.8 \leqslant z < 3.0$.

The full band X-ray flux spans more than three orders of magnitude, ranging between 3 and 6950 $\times 10^{-17}$ erg cm^{-2} s^{-1}, with a median flux of 87 $\times 10^{-17}$ erg cm^{-2} s^{-1}. The hard-band X-ray-detected sources span a smaller range in flux, spanning between 9 and 4230 $\times 10^{-17}$ erg cm^{-2} s^{-1}, with a median flux of 135 $\times 10^{-17}$ erg cm^{-2} s^{-1}.

2.3. Optical and Near-infrared Imaging

The ≈160 arcmin^2 GOODS-N field has been imaged extensively at optical wavelengths using the ACS camera on the *Hubble Space Telescope* in the following four filters: B_{435}, V_{606}, i_{775}, and z_{850} (Giavalisco et al. 2004). In our analysis, we use the catalogs for version 1 of the ACS data obtained from MAST. Additional ground-based imaging of GOODS-N in the *U* band was obtained using the prime-focus MOSAIC camera on the KPNO Mayall 4 m telescope. A subset of these data was described in Giavalisco et al. (2004) and Capak et al. (2004); the present analysis uses a version of the *U*-band data that have approximately twice the exposure time. The *U*-band photometry was measured by detecting sources in the Subaru *R*-band image of Capak et al. (2004) and measuring *U*-band fluxes through matched apertures. Sources were considered detections in the *UBViz* bands if they had an S/N > 3, corresponding to a typical detection limit of 0.050, 0.035, 0.024, 0.035, and 0.026 μJy, respectively.

GOODS-N has also been observed at near-infrared (NIR) wavelengths with the Wide-Field Near Infrared Camera (WIRCAM) at the Canada–France–Hawaii Telescope (CFHT), including K_s-band observing programs from Hawaiian and Canadian observing programs, and *J*-band data from a Taiwanese program. WIRCAM has a field of view covering 21.′5 × 21.′5, fully encompassing the GOODS-N ACS, IRAC, and MIPS areas. Here, we use reductions of the WIRCAM data from L. Lin et al. (2011, in preparation), consisting of 27.4 hr of integration time at *J* and 31.9 hr at K_s. The images have seeing with a typical FWHM of ≈0.″7. Sources were considered detections at *J* and K_s if they had an S/N > 3 and a flux density larger

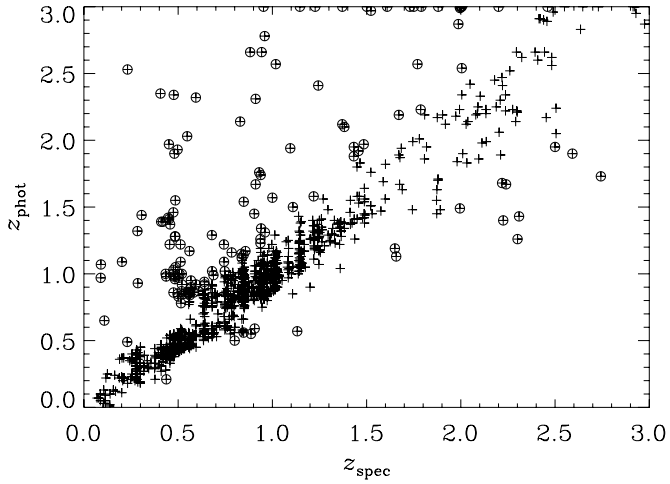

Figure 3. Comparison between the photometrically recovered redshifts to the spectroscopic values. The distribution of relative errors $dz = (z_{phot} - z_{spec})/(1 + z_{spec})$ has a median of $\approx -0.005 \pm 0.186$. Outliers (i.e., those sources having $|dz| > 0.15$) are identified with open circles. Excluding these sources reduces the median and dispersion of the distribution of relative errors to $\approx 0.003 \pm 0.058$.

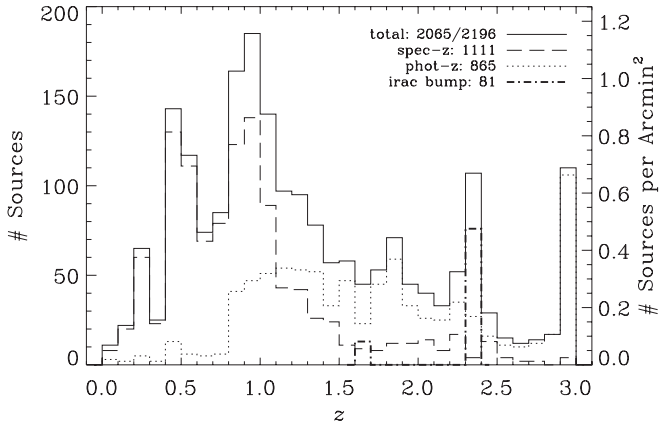

Figure 4. Histogram of the redshift distribution for 24 μm sources included in the ACS areal coverage. The maximum allowed photometric redshift is set to $z_{phot} = 3$; such sources were not used in our analysis of the evolution of the infrared luminosity density vs. redshift. There are six sources with $z_{spec} \geqslant 3$ not shown.

than 0.312 and 0.456 μJy, respectively. An independent analysis of the WIRCAM K_s-band data has recently been published by Wang et al. (2010).

IRAC data at 3.6, 4.5, 5.8, and 8.0 μm were taken as part of the GOODS *Spitzer* Legacy program (M. Dickinson et al. 2011, in preparation). The formal 3σ limits for an isolated point source are 0.079, 0.137, 0.867, and 0.951 μJy for channels 1, 2, 3, and 4, respectively. However, in practice, the signal to noise will depend on the degree of crowding with other nearby sources.

2.4. Inclusion of Photometric Redshifts

The 24 μm detections were cross-matched against the ACS *BViz*, CFHT JK_s, and the 3.6 and 4.5 μm IRAC catalogs to provide photometric input for the Z-PEG code (Le Borgne & Rocca-Volmerange 2002) to compute photometric redshifts. Only sources having detections (i.e., S/N $>$ 3) in four or more of these wavebands are considered to have reliable photometric redshifts. A maximum redshift value of 3 was used while running Z-PEG. The distribution of relative errors $dz = (z_{phot} - z_{spec})/(1 + z_{spec})$ among the 1050 sources having spectroscopic and photometric redshifts has a median and dispersion of $\approx -0.005 \pm 0.186$ (Figure 3). Applying an outlier criterion of $|dz| > 0.15$, which excludes 139 ($\approx$13%) of the sources, the median and dispersion of the relative errors are reduced to $\approx 0.003 \pm 0.058$.

Using all 1050 sources (i.e., including $|dz| > 0.15$ outliers), we assign uncertainties to the photometric redshifts by taking the standard deviation of the difference between the spectroscopic and photometric redshifts ($\sigma_{\Delta z}$) within each of the last five redshift bins listed in Table 2 resulting in uncertainties of $z \pm 0.33$, 0.27, 0.28, 0.46, and 0.46, respectively. These values, in addition to the uncertainties on the input flux densities in the SED fitting, were used in a Monte Carlo approach when estimating uncertainties on IR luminosities derived with photometric redshifts (see Section 3.1.1).

For an additional 81 sources not having enough broad-band detections to extract a reliable photometric redshift using Z-PEG, we use their peak in the IRAC channels to place them into a redshift bin based on the expected location of the 1.6 μm stellar bump. Taking the updated Bruzual & Charlot (2003) stellar templates, which include a revised prescription for stars on the asymptotic giant branch (AGB; see Bruzual 2007), extincted by an $A_V = 1$, it is found that the 1.6 μm stellar bump should shift into IRAC channels 2 and 3 for redshift bins of $1.3 \lesssim z \lesssim 1.9$ and $1.9 \lesssim z \lesssim 2.8$, respectively. For these sources, the center of the redshift bins is used when calculating IR luminosities (i.e., $z \approx 1.6$ and 2.35, respectively). Uncertainties in these redshifts were estimated by taking the standard deviation of the difference between the spectroscopic and IRAC-based photometric redshifts where possible, resulting in uncertainties of $z \approx 1.6 \pm 0.47$ and $z \approx 2.35 \pm 0.69$. The choice of an $A_V = 1$ was for simplicity; we note that by increasing the assumed extinction to an $A_V = 3$, the center of the redshift bins decreases to $z \approx 1.44$ and 2.19, resulting in IR luminosities which are $\approx$20% and 35% smaller, respectively, which is within our estimated errors.

As with the IR luminosities derived using photometric redshifts above, uncertainties in the IRAC-based photometric redshifts were used to assign an additional uncertainty to the IR luminosity through a standard Monte Carlo technique. The redshift distribution for the 2065 (out of 2196) 24 μm-selected sources included in the ACS areal coverage, for which we have a spectroscopic or photometric redshift, is shown in Figure 4. The inclusion of these photometric redshifts results in a redshift completeness of $\approx$94%. We note here that photometric redshifts are only used for our analysis of the evolution of the IR luminosity density versus redshift.

3. ESTIMATING STAR FORMATION AND AGN ACTIVITY

In the following section, we briefly describe our methods for calculating IR (8–1000 μm) luminosities (L_{IR}) for each 24 μm-detected source. In addition, we describe a method to estimate the AGN contribution to each IR luminosity. IR luminosities are used to estimate corresponding SFRs following the conversions given in Kennicutt (1998). The analysis presented here closely follows that of Murphy et al. (2009), where a more detailed description can be found; in Appendix A we present a similar comparison of IR, radio, and UV (1500 Å) based SFRs, while in Appendix B we demonstrate that the bolometric and AGN corrections given in Murphy et al. (2009) are applicable to the present study of 24 μm-selected galaxies. All calculations

are made assuming a Hubble constant of $71\,\mathrm{km\,s^{-1}}$, and a standard ΛCDM cosmology with $\Omega_M = 0.27$ and $\Omega_\Lambda = 0.73$. Throughout the paper, average properties are measured by taking a median rather than a mean.

3.1. Estimating IR Luminosities of Galaxies

In the following subsection, we describe our methodology for deriving estimates of the IR luminosities among the sample. We also describe how we account for the fractional contribution of AGN to the IR luminosity of each source.

3.1.1. Determining IR Luminosities from SED Fitting

We fit the photometric data (i.e., the 16, 24, and 70 μm flux densities where available) with the SED templates of Chary & Elbaz (2001) and then integrate between 8 and 1000 μm. The SED libraries of Chary & Elbaz (2001) are used since they have recently been found to exhibit 24/70 μm flux density ratios which are better matched to the average observed for galaxies at $z \sim 1$ compared to the Dale & Helou (2002) or Lagache et al. (2003) templates (Magnelli et al. 2009). The best-fit SEDs are determined by a χ^2-minimization procedure in which the amplitude (luminosity) and shape (temperature) of SED templates are allowed to scale freely. Fitting errors are estimated by a standard Monte Carlo approach using the photometric uncertainties of the input flux densities, as well as redshift uncertainties for sources having only photometric redshifts. In the cases where only upper limit values are available for the photometric data, they are not incorporated into the formal χ^2 minimization but are used to reject fits having associated flux densities greater than the upper limit. These IR luminosities are identified by $L_{\rm IR}^{16,24,70}$.

For sources without far-infrared information (i.e., those sources not detected at 70 μm), which constitutes the majority of sources, $L_{\rm IR}^{16,24,70}$ values are estimated by averaging the IR luminosities from the best-fit Chary & Elbaz (2001) and Dale et al. (2001) SEDs. Since the Dale et al. (2001) SED templates are not normalized by luminosity, we do so using a local trend between IRAS colors and IR luminosity as the Dale et al. (2001) SEDs are described by a single parameter (i.e., $f_\nu(60\,\mu\mathrm{m})/f_\nu(100\,\mu\mathrm{m})$) family. Due to the non-detection at wavelengths close to the peak of the far-infrared emission, the IR luminosities of such sources may be considered as upper limits. We note that for a heterogeneous sample (i.e., submillimeter galaxies (SMGs), AGNs, and optically faint sources) of 22 galaxies spanning the same redshift range being probed here, IR luminosities derived in this manner were found to be $\sim 1.0 \pm 0.5$ times those estimated from SED fitting with additional mid-infrared spectra and (for 18 of the 22 galaxies) 70 and/or 850 μm photometry (Murphy et al. 2009).

We additionally calculate IR luminosities by fitting SEDs with the 24 μm photometry alone. This is also done by fitting both the Chary & Elbaz (2001) and Dale et al. (2001) SED template libraries independently, and averaging their integrated 8–1000 μm luminosities. The associated IR luminosity is designated as $L_{\rm IR}^{24}$, and is, on average, within $\lesssim$5% of those derived from fitting either set of SED templates. The difference between the resultant $L_{\rm IR}^{24}$ from the two sets of SED templates is characterized as a systematic error.

3.1.2. Empirical Correction for 24 μm-derived IR Luminosities

Murphy et al. (2009) have shown that IR luminosities derived by fitting local SEDs with 24 μm photometry alone typically overestimate the true IR luminosity by an average factor of ∼5 among sources having $z > 1.4$ and $L_{\rm IR}^{24}$ values $\gtrsim 3 \times 10^{12}\,L_\odot$. We use that result to derive an empirical correction for $L_{\rm IR}^{24}$. In the left and right panels of Figure 5, we plot the ratio of 24 μm-derived to best-fit IR luminosities ($L_{\rm IR}^{16,24,70}$) for all of the 70 μm-detected sources having spectroscopic redshifts, versus redshift and 24 μm-derived IR luminosities, respectively. Also included in each panel is the ratio of 24 μm-derived to best-fit IR luminosities for 18 galaxies presented by Murphy et al. (2009); the IR luminosities among these galaxies were fit using 70 and/or 850 μm photometry and are considered fairly well determined. For the nine 70 μm-detected sources which overlap between the IRS and larger GOODS-N samples, we use the IR luminosity reported by Murphy et al. (2009) because those estimates include the mid-infrared spectroscopic data in the fits.

The trend reported by Murphy et al. (2009) appears to hold. The 24 μm-derived IR luminosities of galaxies having redshifts between $1.4 \lesssim z \lesssim 2.6$ and $L_{\rm IR}^{24} \gtrsim 3 \times 10^{12}\,L_\odot$ are overestimated by an average factor of $\sim 4.6 \pm 1.7$. Galaxies at lower redshifts, having $L_{\rm IR}^{24} < 10^{12}\,L_\odot$, have 24 μm-derived IR luminosities which are consistent with our best-fit determinations using additional longer wavelength data. These results are also consistent with recent *Herschel* findings confirming the reported overestimates in 24 μm-derived IR luminosities by Murphy et al. (2009; i.e., Elbaz et al. 2010; Nordon et al. 2010).

While trends exist between the overestimates in the bolometric correction for both redshift and 24 μm-derived IR luminosity (see right panel of Figure 5), we believe the latter to be the dominant parameter as the trend between the ratio of 24 μm-derived to best-fit IR luminosity versus 24 μm-derived IR luminosity appears tighter than versus redshift; the residual dispersion in the fit between the ratio of 24 μm-derived to best-fit IR luminosity and redshift (for $z \gtrsim 1.3$) is ∼40% larger than the fit versus luminosity, where $L_{\rm IR}^{24} \geqslant 10^{12}\,L_\odot$. Furthermore, individual lensed Lyman break galaxies (LBGs) at $z \sim 2.5$, having IR luminosities $\lesssim 10^{12}\,L_\odot$, appear to show bolometric corrections that are similar to those of local galaxies (Siana et al. 2008; Wilson et al. 2008; Gonzalez et al. 2009).

Consequently, we correct the 24 μm-derived IR luminosities using this information. For galaxies having $L_{\rm IR}^{24} < 10^{12}\,L_\odot$, we do not apply a correction given that the median ratio of $L_{\rm IR}^{24}$ to the best-fit IR luminosity is 1.1 ± 0.27. For galaxies having $L_{\rm IR}^{24} > 10^{12}\,L_\odot$, we apply an empirical correction by fitting these sources with an ordinary least-square regression such that

$$\log\left(\frac{L_{\rm IR}^{24,\rm corr}}{L_\odot}\right) = \begin{cases} \log\left(\frac{L_{\rm IR}^{24}}{L_\odot}\right), & L_{\rm IR}^{24} < 10^{12}\,L_\odot \\ (0.60 \pm 0.04)\log\left(\frac{L_{\rm IR}^{24}}{L_\odot}\right) + (4.8 \pm 0.5), & L_{\rm IR}^{24} \geqslant 10^{12}\,L_\odot. \end{cases} \quad (1)$$

For the cases where these IR luminosity estimates exceed those derived using the additional 16 and 70 μm data, we take the minimum value between these two values as the best estimate for the true IR luminosity of each source such that

$$L_{\rm IR} = \min\left(L_{\rm IR}^{24,\rm corr}, L_{\rm IR}^{16,24,70}\right). \quad (2)$$

The fraction of cases for which $L_{\rm IR}^{24,\rm corr}$ was much larger

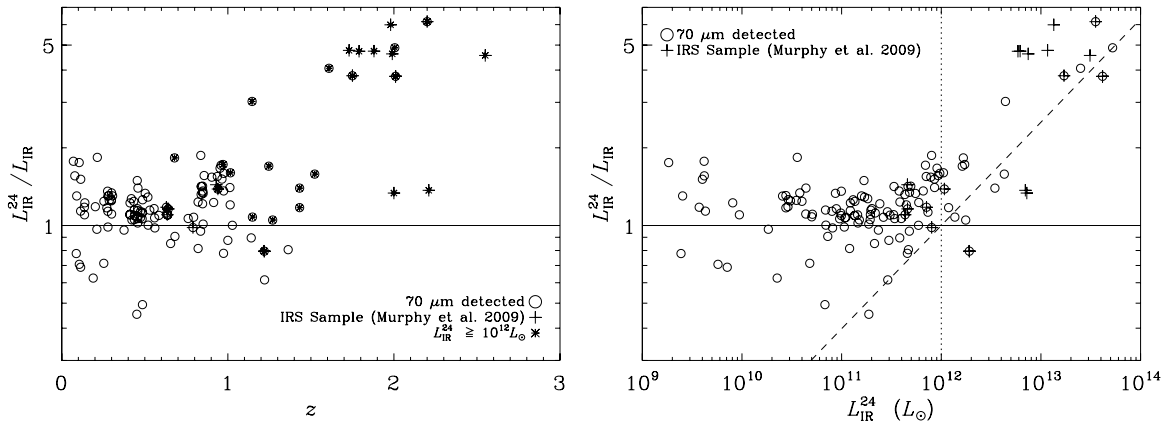

Figure 5. In the left panel, we plot the ratio of the 24 μm-derived IR luminosity to those estimated by SED template fitting with the 16, 24, and 70 μm photometry for all 70 μm detections (open circles) vs. redshift. Also included is the ratio of the 24 μm-derived to the best-fit IR luminosities for the mid-infrared spectroscopic sample of Murphy et al. (2009, plus symbols). ULIRGs ($L_{\rm IR} \geqslant 10^{12}\,L_{\odot}$) are identified by asterisks. In the right panel, we plot the same ratios against the 24 μm-derived IR luminosity. The vertical dotted line separates ULIRGs from non-ULIRGs and the dashed line is the ordinary least-squares fit to the ULIRGs given by Equation (1).

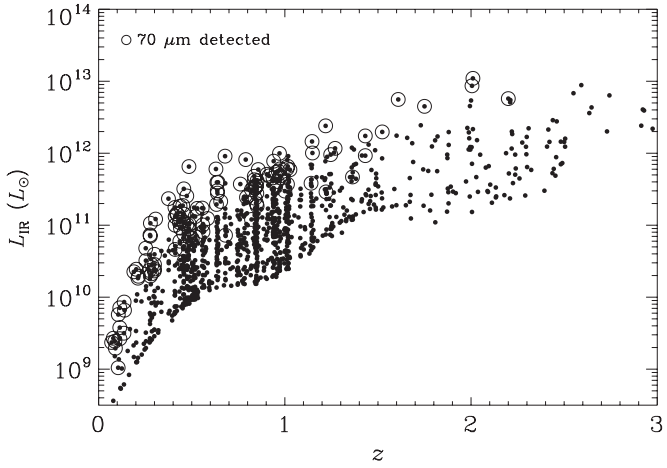

Figure 6. Best-fit IR luminosities for each of the 1107 24 μm detections having spectroscopic redshifts of $z < 3$. Sources detected at 70 μm are identified by an open circle.

than $L_{\rm IR}^{16,24,70}$ (i.e., $L_{\rm IR}^{24,\rm corr}/L_{\rm IR}^{16,24,70} > 2$) occurred for ~2% of the sample. Lastly, for the subsample of 22 sources included in Murphy et al. (2009), we set $L_{\rm IR}$ to their best-fit IR luminosities.

The best-fit IR luminosities are plotted in Figure 6 as a function of redshift for all 1107 24 μm-detected sources having spectroscopic redshifts of $z < 3$. The values range from 2.5×10^8 to $1.1 \times 10^{13}\,L_{\odot}$, spanning more than four orders of magnitude, with a median of $7.2 \times 10^{10}\,L_{\odot}$. Limiting these to galaxies having firm 70 μm detections, the median is increased by a factor of ~2.5 to $1.8 \times 10^{11}\,L_{\odot}$ and the range decreases to 1.0×10^9–$1.1 \times 10^{13}\,L_{\odot}$. On the other hand, the range of the 24 μm-derived luminosities, spans more than five orders of magnitude from 2.7×10^8 to $6.4 \times 10^{13}\,L_{\odot}$, with a median value of $7.6 \times 10^{10}\,L_{\odot}$, roughly the same as the median of the best-fit IR luminosities.

3.1.3. Constraints on AGN Fractions of IR Luminosities

We make a statistical correction to the IR luminosities of each source by assigning a fractional contribution from AGN based on an empirical trend between AGN luminosity and the difference between the 24 μm-derived and true IR luminosities (Murphy et al. 2009) such that

$$\log\left(\frac{L_{\rm IR}^{\rm AGN}}{L_{\odot}}\right) = (0.73 \pm 0.08)\log\left(\frac{L_{\rm IR}^{24}}{L_{\odot}}\right) + (2.5 \pm 1.0). \quad (3)$$

This relation relies on AGN luminosity estimates derived by first decomposing mid-infrared spectra into star formation (PAH template) and AGN (hot dust emission) components. Since hot dust associated with vigorous star formation may also contribute to the mid-infrared continuum emission along with AGN, our estimates for the AGN luminosity could be considered upper limits. However, this conclusion assumes that our choice of AGN template (i.e., Mrk 231) is appropriate for all sources, which may not be the case. Furthermore, it is currently unclear as to whether the far-infrared luminosity of Mrk 231 is powered primarily by AGN (e.g., Armus et al. 2007; Veilleux et al. 2009; Fischer et al. 2010) or star formation (e.g., Downes & Solomon 1998; Farrah et al. 2003). If the latter is true, than that would again argue for the AGN IR luminosity estimates being upper limits. Correspondingly, the SFR density that we have derived would be increased by this amount. However, there is no reason to believe that these high-z sources do not contain AGN which contribute significantly to powering the observed dust emission. Galaxies with SFRs of $\sim 20\,M_{\odot}\,{\rm yr}^{-1}$ typically have stellar masses of $\sim 10^{10}\,M_{\odot}$ (Daddi et al. 2007b) which should therefore harbor black holes of mass $\sim 10^7$–$10^8\,M_{\odot}$ if the black hole–stellar mass relation holds at $z \sim 1$–2 (McLure et al. 2006). Thus, our AGN estimates may be considered upper limits, but in reality it is challenging to definitively quantify this without a precise knowledge of the AGN SED.

By subtracting these values from our best estimates for the true IR luminosity, we can quantify the amount of IR luminosity arising from star formation alone such that $L_{\rm IR}^{\rm noAGN} = L_{\rm IR} - L_{\rm IR}^{\rm AGN}$. For the cases in which this empirical correction leads to AGN contributions that are larger than a source's estimated IR luminosity, we assume the source is completely powered by an AGN and set $L_{\rm IR}^{\rm AGN} = L_{\rm IR}$.

3.2. The Evolution of the IR Luminosity Density versus Redshift

Taking these improved estimates for the total IR luminosity of our 24 μm-selected sample of sources, we can investigate the evolution of the IR luminosity density $\rho_{L_{\rm IR}}$ as a function of redshift. We do this in five different redshift bins between

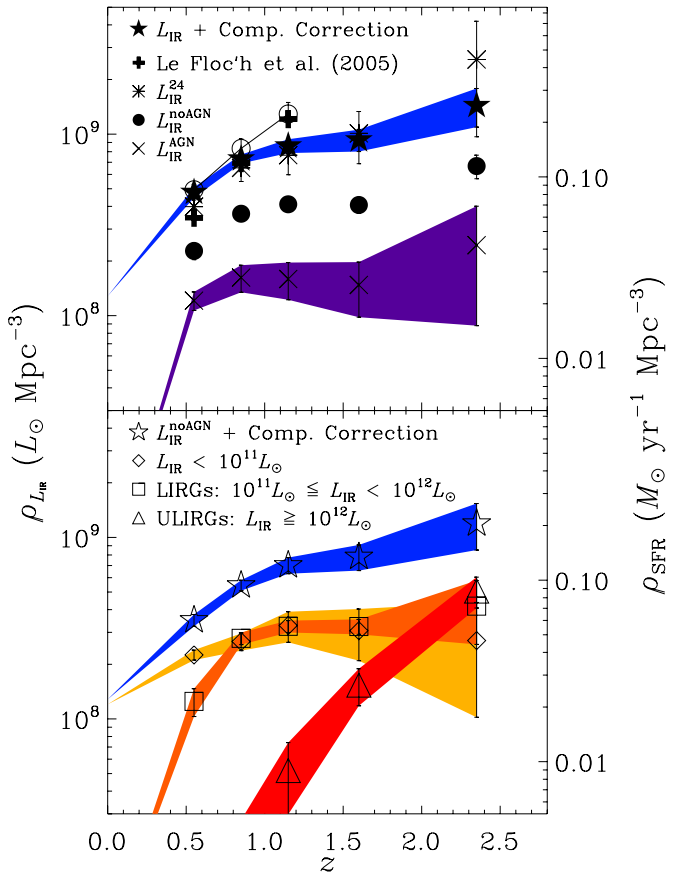

Figure 7. Evolution of the co-moving star-formation- and accretion-driven IR luminosity densities with redshift. In the top panel, we plot $\rho_{L_{IR}}$ calculated using 24 μm based IR luminosities (asterisks) and our best-fit IR luminosities, fit using our other photometric data, after subtracting an estimate of the AGN contribution to the total IR luminosity (filled circles). An estimate of the AGN luminosity density is shown as crosses, which can be considered an upper limit. The total IR luminosity density (i.e., before subtracting out an estimate of the AGN contribution), corrected for sources below our sensitivity limits using the luminosity function work of Magnelli et al. (2011), is given by filled stars in the top panel (see Section 3.2.1). For comparison with other work, we plot the IR luminosity density estimates of Le Floc'h et al. (2005, bold plus symbols) for our first three redshift bins; correcting our 24 μm-derived IR luminosities with their IR luminosity functions (open circles), we find that our 24 μm-derived IR luminosity density values agree, but are significantly above our best-fit SFR density determinations. In the bottom panel, we show the total star-formation-driven IR luminosity density (i.e., after subtracting out an estimate of the AGN contribution), which has been corrected for sources below our sensitivity limits, as open stars. We also show the relative contributions to the star-formation-driven IR luminosity density (i.e., AGN corrected), calculated using all available photometric data, arising from low-luminosity galaxies (diamonds), LIRGs (squares), and ULIRGs (triangles). Sources are classified by their total IR luminosity (i.e., including any AGN contribution). The $z = 0$ data point for the total IR luminosity density, along with contributions from normal galaxies, LIRGs, and ULIRGs, was measured by integrating the $z = 0$ luminosity function of Magnelli et al. (2009), while the $z = 0$ AGN IR luminosity density was taken from Xu et al. (2001) and corrected for different cosmologies. The shaded regions include the 1σ uncertainties.

(A color version of this figure is available in the online journal.)

$0.4 \leqslant z < 2.8$ (i.e., the last five redshift bins in Table 2). By using our IR luminosity estimates that have been corrected for the presence of extra infrared emission arising from embedded AGN, we convert the IR luminosity density into an SFR density ρ_{SFR} to examine the evolution of the star formation history of the universe over the last $\sim$11.3 Gyr (see Figure 7 and Table 3). In this analysis, we only consider 24 μm sources included in the areal coverage of the ACS imagery since these were the sources targeted for spectroscopic redshifts. The angular area of this region on the sky is approximately 160 arcmin^2. A detailed discussion of the evolution of the star-formation- and accretion-driven IR luminosity densities with redshift using our new results can be found in Section 5.

3.2.1. Completeness Corrections for the Faint End of the Luminosity Function

To correct for the additional luminosity arising from galaxies having 24 μm flux densities below the 24 μm sensitivity limit (i.e., see Figure 6), we employ the luminosity function derived from FIDEL data by Magnelli et al. (2009, 2011). The luminosity function is parameterized by a broken power law, whose evolution flattens once beyond $z \gtrsim 1.3$, being consistent with a luminosity evolution proportional to $(1 + z)^{3.6\pm0.4}$ and $(1 + z)^{1.0\pm0.9}$ below and above $z \approx 1.3$, respectively. The corresponding density evolution for redshifts below and above $z \approx 1.3$ is proportional to $(1 + z)^{-0.8\pm0.6}$ and $(1 + z)^{-1.1\pm1.5}$, respectively. At high redshifts, these corrections will depend on the assumption that the infrared luminosity function has the same logarithmic slope that is measured locally (i.e., Sanders et al. 2003).

By evolving the IR luminosity function appropriately for a given redshift, we integrate the luminosity contribution for galaxies having IR luminosities between $10^7\,L_\odot$ and the IR luminosity corresponding to our 24 μm upper limit of 30 μJy at redshifts spaced by increments of $\Delta z = 0.05$ within each of the five redshift bins between $0.4 \leqslant z < 2.8$. We then averaged the completeness corrections included in each of these redshift bins, weighted by the volume of each redshift increment. This value was then assigned as the effective completeness correction for that redshift bin. The completeness corrections for these redshift bins are $\approx$1.2, 1.8, 2.9. 3.8, and $5.3 \times 10^8\,L_\odot$ Mpc^{-3}, respectively. Similarly, we used this approach when accounting for corrections of galaxies in different luminosity classes (i.e., normal galaxies and LIRGs). The values of the completeness correction for LIRGs per each redshift bin are $\approx$0.0, 0.0, 0.058, 0.70, and $2.6 \times 10^8\,L_\odot$ Mpc^{-3}, respectively. The difference between the total completeness correction and these values correspond to the completeness correction for normal galaxies alone.

In Figure 8, we plot the space density evolution for LIRGs and ULIRGs. Also shown is the completeness-corrected number density for LIRGs using the technique described above. These corrections are $\approx$0.0, 0.0, 0.054, 0.54, and 1.1×10^{-3} Mpc^{-3}, respectively.

3.2.2. Propagations of Errors for IR Luminosity Densities

There are four primary sources of uncertainty in estimating the IR luminosity densities: photometric redshifts, photometric uncertainties, bolometric corrections, and completeness corrections. These are derived using a Monte Carlo technique from both photometry, and where applicable, the photometric redshift. The additional uncertainty of the scatter in our empirical correction for the overestimation of the 24 μm-derived IR luminosities, which is $\approx$27% for sources with $L_{IR}^{24} < 10^{12}\,L_\odot$ and $\approx$42% about the fitted regression line for sources with $L_{IR}^{24} \geqslant 10^{12}\,L_\odot$ (see the right panel of Figure 5) is then added to the fitting errors in quadrature for each galaxy. Similarly, we include an uncertainty for the AGN subtraction based on the residual dispersion (i.e., $\approx$66%) in the empirical correlation (i.e., right panel of Figure 8 in Murphy et al. 2009) used to derive Equation (3). This uncertainty is included in the quadrature sum above.

Table 3
Star Formation and Accretion Powered IR Luminosity Density Evolution

Redshift	$\rho_{L_{IR}}$	ρ_{SFR}[a]	ρ_{AGN}[b]	LIRGs		ULIRGs
				$L_{IR} < 10^{11}\ L_\odot$	$10^{11}\ L_\odot \leqslant L_{IR} < 10^{12}\ L_\odot$	$L_{IR} \geqslant 10^{12}\ L_\odot$
	($10^8\ L_\odot\ Mpc^{-3}$)	($M_\odot\ yr^{-1}\ Mpc^{-3}$)	($10^8\ L_\odot\ Mpc^{-3}$)	(%[c])	(%[c])	(%[c])
$0.4 \leqslant z < 0.7$	4.78 ± 0.31	0.062 ± 0.005	1.21 ± 0.14	63	35	2
$0.7 \leqslant z < 1.0$	7.31 ± 0.41	0.098 ± 0.006	1.62 ± 0.28	47	49	4
$1.0 \leqslant z < 1.3$	8.62 ± 0.76	0.122 ± 0.012	1.59 ± 0.37	47	46	7
$1.3 \leqslant z < 1.9$	9.30 ± 1.28	0.135 ± 0.022	1.48 ± 0.50	39	41	20
$1.9 \leqslant z < 2.8$	14.39 ± 3.45	0.207 ± 0.059	2.44 ± 1.56	23	35	42

Notes.
[a] $\rho_{SFR}(M_\odot\ yr^{-1}\ Mpc^{-3}) = 1.73 \times 10^{-10}[\rho_{L_{IR}}(L_\odot\ Mpc^{-3}) - \rho_{AGN}(L_\odot\ Mpc^{-3})]$.
[b] These values for the AGN IR luminosity density may be considered as upper limits (see Section 3.1.3).
[c] Percentage of the SFR density.

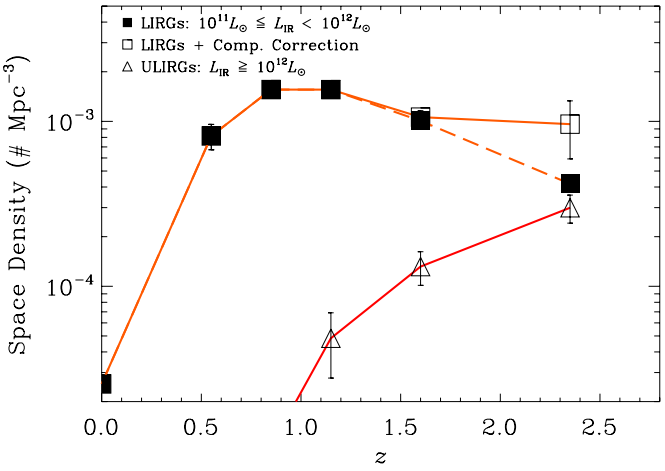

Figure 8. Space density evolution of 24 μm-selected LIRGs (squares) and ULIRGs (triangles). The contribution from LIRGs before applying a completeness correction (see Section 3.2.1) is given by the filled squares. Values at $z = 0$, along with the first two redshift bins for which we do not detect ULIRGs (i.e., $z = 0.55$ and 0.85) were taken from Magnelli et al. (2009).
(A color version of this figure is available in the online journal.)

The uncertainty in the completeness corrections for the faint end of the luminosity functions is based on the dispersion in the bolometric corrections (observed-frame $L_{IR}/\nu L_\nu(24\ \mu m)$ ratios at each redshift bin between $0.4 \leqslant z < 2.8$ in Table 2) for the Chary & Elbaz (2001) templates. Assuming effective dust temperatures of $T_{dust} = 36 \pm 7$ K, and a dust grain emissivity of $\beta_{dust} = 1.6$ (e.g., this temperature range has been estimated from average galaxy SEDs at these redshifts; Dye et al. 2007), we find that the corresponding bolometric correction uncertainties are 8%, 16%, 21%, 32%, and 62% for each redshift bin, respectively. These uncertainties are then added in quadrature to the uncertainties on the total IR luminosity density of each redshift bin, which was based on the propagation of the uncertainties on the IR luminosities of each source included in that redshift bin. The shaded regions plotted in Figure 7 illustrate the 1σ uncertainties.

4. COMPARISON BETWEEN IR AND EXTINCTION-CORRECTED UV SFRs FOR 24 μm-SELECTED SOURCES

Having our improved estimates for IR luminosities, we now look to see how well local extinction corrections, based on the UV spectral slope, work for our sample of 24 μm-selected galaxies. A full treatment investigating local extinction corrections among 24 μm-selected galaxies in the *BzK* redshift range can be found in Appendix C.

4.1. Typical Correction for UV Extinction

UV-based SFRs (SFR_{UV}) are calculated using the rest-frame 1500 Å specific luminosities for each source using the *UBViz* photometry and the conversion given in Kennicutt (1998) as described in Murphy et al. (2009). We estimate the amount of extinction at 1500 Å using the empirical relation between the UV spectral slope spanning 1250–2600 Å, defined as β, to the total amount of extinction at 1600 Å (Meurer et al. 1999), along with modeled extinction curves (i.e., Weingartner & Draine 2001; Draine 2003), such that,

$$\left(\frac{A_{1500}}{\text{mag}}\right) = 4.65 + 2.09\beta. \quad (4)$$

Since the redshifts of the sample galaxies are at $z < 3$, any correction to the UV slope due to absorption by the intergalactic medium is likely negligible. Sources having $\beta < -3$ or $\beta > 2$ are excluded in this analysis as this is outside the range for which the UV spectra slope has been calibrated to extinction. These sources were generally those having (low) redshifts for which β was determined using two data points that included the ground-based *U*-band data, which are less sensitive and have much coarser resolution than the ACS imaging. The minimum redshift for which we have calculated a reliable extinction correction UV luminosity is $z \approx 0.66$. Extinction-corrected UV SFRs are denoted as SFR_{UV}^{corr}.

4.2. Applicability to 24 μm-detected Sources

In Figure 9, we plot the ratio of IR+UV to UV-corrected SFRs versus the estimated $E(B-V)$ color excesses (i.e., $E(B-V) = 0.123A_{1500}$). For these comparisons with the UV SFRs, IR luminosities have not been corrected for the presence of AGN, however using the AGN subtracted values does not significantly affect the results. We note that the minimum redshift among these sources, where we could obtain a reliable estimate of the UV spectral slope, is $z \approx 0.66$. We have also limited this comparison to sources with $z < 2.6$. The UV-corrected SFRs appear to be overestimated by more than a factor of $\gtrsim$2, on average, among the 24 μm-selected sources plotted, and we see a clear trend of decreasing ratio of IR + UV to UV-corrected SFRs with increasing extinction suggesting that the UV slope is overestimating the extinction in a large number of sources.

The fact that there is a trend at all suggests that the treatment for extinction correcting the UV flux densities is not adequate

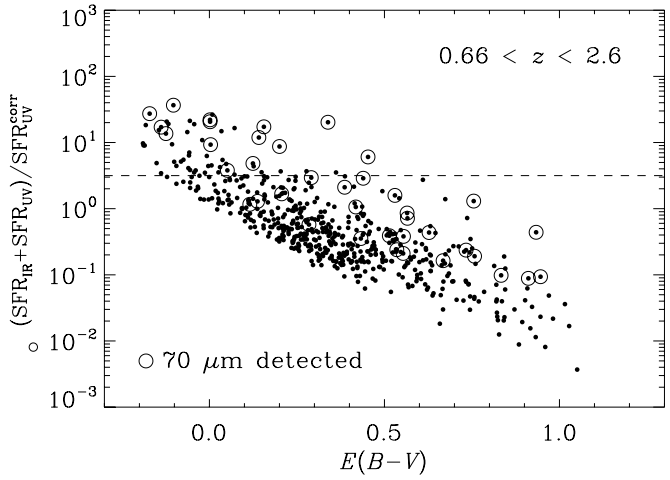

Figure 9. We plot the ratio of IR derived SFRs estimated from SED fitting (plus UV-derived SFRs uncorrected for extinction) to extinction-corrected UV SFRs against the color excess $E(B-V)$ inferred from fitting the rest-frame UV (1250–2600 Å) slope using *UBViz* optical imaging data; those galaxies which are 70 μm-detected are identified with circles. IR luminosities have not been corrected for AGN contributions, which makes little difference for the observed trend.

for our sample. To quantify this, we plot an estimate of A_{1500}, which is derived from the ratio of the total (IR + observed UV) to the observed UV SFR, against the UV spectral slope, β (see the left panel of Figure 10). A clear trend of increasing extinction with β is found, for which an ordinary least-squares fit results in the relation

$$\left(\frac{A_{1500}}{\mathrm{mag}}\right) = 2.75 \pm 0.06 + (0.75 \pm 0.04)\beta. \quad (5)$$

Our sample of 24 μm-selected galaxies typically falls well below the UV extinction correction of Meurer et al. (1999; i.e., Equation (4)), which is plotted as a dashed line.

Taking these revised estimates for the UV extinction, we correct our UV luminosity and derive revised UV-corrected SFRs ($\mathrm{SFR}_{\mathrm{UV}}^{\mathrm{rev-corr}}$). In the right panel of Figure 10, we plot the IR + (observed) UV SFRs against the revised, extinction-corrected UV SFRs which exhibits a general one-to-one trend, albeit with a significant amount of (factor of ∼3) scatter. Also shown in the right panel of Figure 10 is the result from fitting the IR + (observed) UV SFRs with the extinction-corrected UV SFRs using the relation taken from Meurer et al. (1999). A clear discrepancy is found between these two fits suggesting that the extinction correction prescription given by Meurer et al. (1999) is not appropriate for our sample of 24 μm-selected sources. Extinction-corrected UV luminosities are a factor of ≈2 larger using the local (starburst) relation of Meurer et al. (1999, i.e., Equation (4)) compared to our revised values using Equation (5).

We believe this result may arise in part due to the age-extinction degeneracy among the lower redshift (i.e., $0.66 \lesssim z \lesssim 1.4$) objects in our sample. Attenuation relations flatter than that of Meurer et al. (1999) have also been reported for samples of "normal" star-forming galaxies (e.g., Bell 2002; Kong et al. 2004; Buat et al. 2005), 250 μm-selected galaxies at $z < 1$ (Buat et al. 2010), as well as UV-selected $z \sim 1$ galaxies when comparing to stacked X-ray SFRs (Laird et al. 2005). If the extinction is relatively lower in these objects, the UV slope will no longer be as sensitive to the amount of extinction due to the importance of variations arising from contributions by a galaxy's old stellar population. Another explanation for a flatter attenuation relation could be due to a steeper UV extinction curve among our sample of 24 μm-selected sources. While most normal $z \sim 2$ LBGs (i.e., UV-selected starbursts with $10^{10}\,L_{\odot} \lesssim L_{\mathrm{IR}} \lesssim 10^{12}\,L_{\odot}$) follow the Meurer et al. (1999) relation, young ($\lesssim$100 Myr) LBGs tend to fall below the local starburst relation which has been attributed to a steeper, more SMC-like, UV extinction law in these sources (Reddy et al. 2006, 2010). This physical effect may also play a role in placing

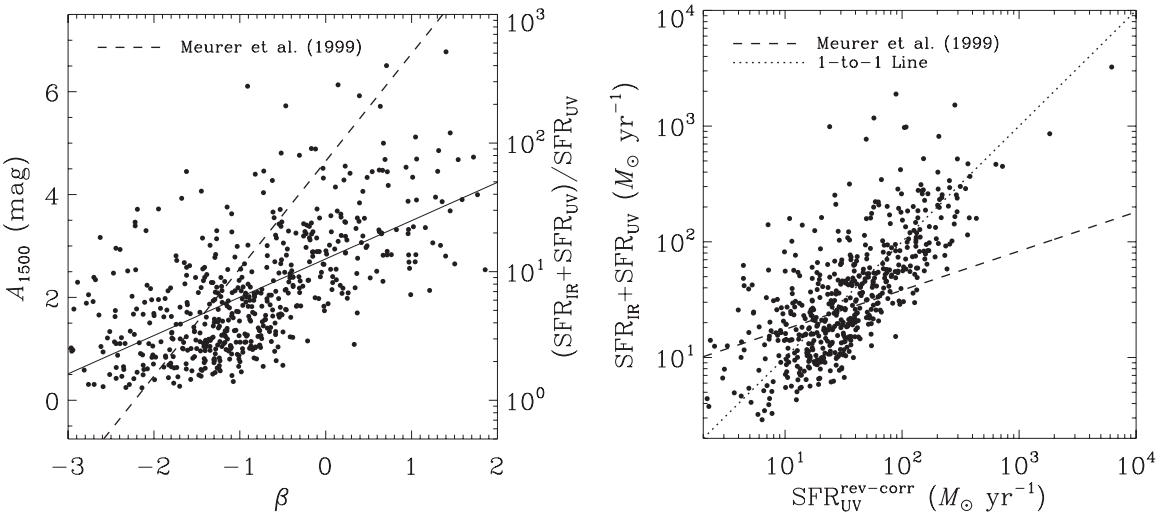

Figure 10. In the left panel, we plot our estimate of A_{1500}, which is derived from the ratio of the total (IR + observed UV) to the observed UV SFR, against the measured UV spectral slope, β, for those galaxies shown in Figure 9. As in Figure 9, IR luminosities have not been corrected for AGN contributions. The overplotted solid line is the ordinary least-squares fit to A_{1500} vs. β (Equation (5)), while the dashed line indicates the UV extinction correction of Meurer et al. (1999, i.e., Equation (4)). In the right panel, we plot the total (IR + observed UV) SFR against our revised extinction-corrected UV SFRs using the fit from the left panel. The dotted line is a one-to-one line. The dashed line indicates the fit to the IR + observed UV SFR vs. the UV-corrected SFR when using the UV spectral slope to correct for reddening given by Equation (4). This discrepancy clearly shows that the UV extinction correction using Meurer et al. (1999) is not appropriate for this sample of 24 μm-selected sources.

our sample of 24 μm-selected galaxies below the Meurer et al. (1999) relation in the left panel of Figure 10.

5. DISCUSSION

Following the results of Murphy et al. (2009), we use deep imaging at 70 μm of GOODS-N, as part of the FIDEL survey, to calculate the IR luminosities for 24 μm-detected sources. Using our improved bolometric corrections and estimates for the contribution of AGN (see Section 3.1), we characterize the evolution of the star formation and AGN powered IR luminosity density out to $z \sim 2.8$.

5.1. Uniqueness of Sample and Analysis

Here, we highlight the major differences between our work for deriving the co-moving SFR and accretion energetics over the past ~11 Gyr compared to others in the literature. First, we are working with a complete sample of 24 μm-selected sources derived from the deepest 24 μm imaging carried out by *Spitzer*. The fact that these observations were taken for the GOODS-N field provides a treasury of optical and NIR ancillary data for assigning redshifts (spectroscopic and photometric) to ≈94% or the sample. Additionally, deep 70 μm, and 850 μm data were available for a subset of the sample, allowing us to estimate the true IR luminosities of each source based on the deep 24 μm photometry alone (i.e., without having to rely on stacking analyses). Deep mid-infrared spectroscopy has allowed us to empirically estimate the fractional AGN contribution to each IR luminosity, resulting in the first measure of obscured AGN energetics with redshift, in addition to measuring contributions to the SFR density as a function of redshift for LIRGs and ULIRGs. Consequently, we have derived a new UV extinction correction based on the measure of the UV spectral slope for 24 μm-selected sources using these new, more accurate estimates for IR luminosity.

5.2. An Accounting of the Star Formation and Accretion Histories to $z \sim 3$

In the top panel of Figure 7, we plot the IR luminosity density versus redshift for galaxies included in the last five redshift bins of the bottom panel of Table 2 (i.e., 24 μm-selected galaxies covered in the ACS imaging). For the directly detected 24 μm sources, we plot independently the contribution from star formation (solid circles) and accretion processes (crosses) to our best-fit IR luminosities. We also plot the IR luminosity density evolution one would predict based on using the 24 μm-derived IR luminosities (asterisks). The corresponding IR luminosity density estimates for our first three redshift bins taken from Le Floc'h et al. (2005) are also given (bold plus symbols); after applying a completeness correction based on their luminosity function work (open circles), we find that our 24 μm-derived IR luminosity density estimates are consistent. However, when the best-fit IR SFR is used (filled stars), we find that the Le Floc'h et al. (2005) results are significantly above our values. This is due to the more precise bolometric correction used in this paper.

We estimate the total and *star-formation-driven* IR luminosity density evolution by including a completeness correction to our best-fit IR luminosities before (top panel; filled stars) and after (bottom panel; open stars) correcting for AGN (see Section 3.2.1); even with the completeness correction, the AGN-corrected values are still well below what the 24 μm-derived IR luminosity density suggests. By using a more robust means of excising out the AGN contribution to the total IR luminosities, our value of the SFR density at $z \approx 2.35$ is $\rho_{\rm SFR} \approx 0.21 \pm 0.06\, M_\odot\ {\rm yr}^{-1}\ {\rm Mpc}^{-3}$. While this value is consistent with that reported by Reddy et al. (2008) for a very similar redshift bin (i.e., $1.9 \leqslant z < 2.7$), these authors did not account for a contribution from AGN. The fractional contribution of AGN to the total IR luminosity density is found to decrease from $\lesssim$25% to $\lesssim$15% with increasing redshift between $0.55 \lesssim z \lesssim 2.35$. On the other hand, the UV-corrected SFR density reported by Reddy et al. (2008), which assumes an average extinction correction of a factor of 4.5, is ≈12% larger than what is derived here.

By averaging the SFR densities in our highest two redshift bins, we obtain a $z \sim 2$ SFR density of $\rho_{\rm SFR} \sim 0.17 \pm 0.06\, M_\odot\ {\rm yr}^{-1}\ {\rm Mpc}^{-3}$ which we can compare to other $z \sim 2$ values quoted in the literature. This value is slightly larger (i.e., ≈15%) than the $z \sim 2$ census value of $0.15 \pm 0.03\, M_\odot\ {\rm yr}^{-1}\ {\rm Mpc}^{-3}$, computed from directly detected (optical, NIR, and submillimeter) galaxies (Reddy et al. 2005), which can be considered a lower limit for the SFR density at this epoch. This value is also ≈50% larger than the $z \sim 2$ SFR density reported by Caputi et al. (2007), which is most likely due to their using a much flatter faint-end slope for their infrared luminosity function as pointed out by a number of authors (e.g., Reddy et al. 2008; Rodighiero et al. 2010; Magnelli et al. 2011).

In the bottom panel of Figure 7, we additionally decompose the star-formation-driven IR luminosity densities into contributions from normal galaxies (diamonds), LIRGs (squares), and ULIRGs (triangles). We note that sources are first separated into IR luminosity classes (normal galaxies, LIRGs, and ULIRGs) based on their total IR luminosity (i.e., the IR luminosity before subtracting out an AGN contribution). By $z \approx 0.85$ there is an equal contribution to the SFR density from normal galaxies and LIRGs. The LIRGs continue to contribute equally with the population of normal galaxies until $z \approx 1.6$, at which point the contribution of normal galaxies begins to decline out to our highest redshift bin at $z \approx 2.35$. We note that the completeness correction, which is unconstrained from the data presented here, is largest for normal galaxies in our highest redshift bin, reflected in the large uncertainties. The trend found for the space density evolution of LIRGs (Figure 8) is slightly different than their luminosity density evolution. The space density of LIRGs appears to peak between $0.85 \lesssim z \lesssim 1.15$ ($\approx (1.6 \pm 0.1) \times 10^{-3}\ {\rm Mpc}^{-3}$) and remains flat until beyond $z \gtrsim 1.15$ where it decreases to $\approx (1.0 \pm 0.4) \times 10^{-3}\ {\rm Mpc}^{-3}$ at $z \approx 2.35$.

The ULIRGs, however, do not appear to account for more than ~20% of the SFR density until redshifts of $z \gtrsim 1.6$, at which point they become roughly comparable with the contribution from LIRGs once beyond $z \gtrsim 2$, contributing at the ≈42% level by $z \approx 2.35$ (see Table 3). Our result is larger than the 30% contribution of ULIRGs to the total SFR density reported by Reddy et al. (2008) in this redshift range (i.e., $1.9 \lesssim z \lesssim 2.8$). On the other hand, the total contribution from LIRGs (37%) and ULIRGs (33%) at $z \sim 2$ is ≈70%, significantly smaller than the ≈93% contribution from LIRGs (48%) and ULIRGs (45%) reported by Rodighiero et al. (2010). Similarly, our result is in contrast with claims that ULIRGs alone dominate the SFR density at $z \sim 2$ (e.g., Pérez-González et al. 2005). We attribute these differences between previous studies to our improved IR luminosity estimates and accounting for AGN, which preferentially affects the most luminous 24 μm sources. In the case of Rodighiero et al. (2010), these authors removed

type-1 quasars in their SFR density calculations, assuming the luminosities of such sources are entirely accretion driven, but did not include a contribution from the bulk of the population as done here; they note that the removal of these sources did not have a large impact on their reported SFR densities, and is thus not the reason for differences between our results.

Similar to Magnelli et al. (2011), we find that the IR luminosity density of LIRGs remains roughly flat between $1.15 \lesssim z \lesssim 2.35$, however we also find the contribution from ULIRGs, and the total SFR density, may increase with redshift over this range. These authors also find that ULIRGs do not dominate the SFR density at $z \sim 2$, albeit they report an even smaller contribution from ULIRGs (i.e., 17%) than the 33% reported here. While ULIRGs appear to contribute significantly to the SFR density at $z \approx 2.35$, we note that the contribution made by ULIRGs to the total SFR density of the universe integrated between $0 \lesssim z \lesssim 2.35$ is small, being ≈20%, where as LIRGs and normal galaxies contribute equally at the ≈40% level. Furthermore, as shown in Figure 8, the space density of ULIRGs is significantly less (i.e., a factor of ≈3) than LIRGs at $z \approx 2.35$.

While the contribution of ULIRGs appears to be large in our final redshift bin, it is not clear that this trend should continue to higher redshifts. Recent work by Magdis et al. (2010) reports on the IR luminosity density of UV-selected ULIRGs at $z \sim 3$, being $\sim 7.5^{+6.5}_{-4.5} \times 10^7\, L_\odot\, \mathrm{Mpc}^{-3}$. This number is significantly smaller than (i.e., ≈15%) our inferred SFR density for $z \approx 2.35$ ULIRGs, and provides a lower limit on the fractional contribution of ULIRGs to the SFR density at $z \sim 3$ since the UV selection is likely to miss more obscured, UV-faint ULIRGs. We also note that the space density of the 24 μm-selected ULIRGs at $z \approx 2.35$ (i.e., $\approx (3.0 \pm 0.6) \times 10^{-4}\, \mathrm{Mpc}^{-3}$) is a factor of ≈20 times larger than the space density of $z \sim 3$ UV-selected ULIRGs reported by Magdis et al. (2010).

It is possible that our final redshift bin may be over predicting the SFR density due to an under estimation of AGN at these epochs since we are assigning the AGN contribution based on a relation which was derived for a heterogenous sample of only ≈20 galaxies (Murphy et al. 2009). However, even by assuming that the IR luminosities estimated for all hard X-ray-detected sources, along with those sources having an IRAC SED described by a power law, are completely AGN powered, this does not flatten the SFR density evolution nor bring the ULIRG contribution below that of the normal galaxies in our highest redshift bin; the SFR density for the final redshift bin decreases to $\rho_{\mathrm{SFR}} \approx 0.19\, M_\odot\, \mathrm{yr}^{-1}\, \mathrm{Mpc}^{-3}$ while the fractional contribution by ULIRGs decreases to ≈39%.

While our results suggest an increase to the IR luminosity density out to $z \approx 2.35$ and that ULIRGs may contribute significantly to the SFR density beyond $z \gtrsim 2$, we note that the uncertainties in our final redshift bin are quite large. Deep surveys with *Herschel*, such as the GOODS-*Herschel* open time key project (PI: D. Elbaz) will likely settle this ambiguity by properly measuring the peak of the FIR SEDs for LIRGs and ULIRGs out to redshifts of $z \sim 2$ and $z \sim 4$, respectively.

6. CONCLUSIONS

In the present study, we have built on the findings of Murphy et al. (2009) to determine how the star-formation- and accretion-driven IR luminosity densities have evolved over the last ≈11.3 Gyr. This has been made possible through improved estimates of IR luminosities, achievable by further constraining fits to local SED templates using deep MIPS imaging at 70 μm taken as part of FIDEL. Our conclusions can be summarized as follows.

1. IR (8–1000 μm) luminosities derived by SED template fitting using observed 24 μm flux densities alone overestimate the IR luminosity by a factor of ∼4 when their 24 μm-derived IR luminosity is $\gtrsim 3 \times 10^{12}\, L_\odot$. This discrepancy appears to be the result of high-luminosity sources at $z \gg 0$ having far- to mid-infrared ratios, as well as aromatic feature equivalent widths, which are more typical of lower luminosity galaxies in the local universe.
2. After accounting for star formation and AGN contributions to the total IR luminosities, we find that AGN and star formation activity appear to roughly track one another with the AGN typically accounting for $\lesssim$18% of the total IR luminosity density integrated between $0 \lesssim z \lesssim 2.35$. The AGN fraction slightly decreases from $\lesssim$25% to $\lesssim$15% with increasing redshift between $0.55 \lesssim z \lesssim 2.35$. Our observations also hint that the star-formation-driven IR luminosity density may increase with redshift between $1.15 \lesssim z \lesssim 2.35$, however, within uncertainties, our results are consistent with a flat evolution over this redshift range.
3. The SFR density (i.e., IR luminosity density corrected for AGN contamination) is dominated by normal galaxies and LIRGs at comparable levels (i.e., each at ≈40%–50%) between $0.85 \lesssim z \lesssim 1.6$. LIRGs continue to contribute at a similar level out to $z \approx 2.35$ which is in contrast with the ULIRGs, which transition to becoming a significant contributor to the SFR density (i.e., comparable with LIRGs) only once beyond $z \gtrsim 2$.
4. Among our sample of 24 μm-selected sources, we find that local prescriptions used to estimate UV extinction corrections based on the UV spectral slope typically overestimate the true extinction by a factor of $\gtrsim$2. Accordingly, using our improved estimates for IR luminosity, we have derived a new UV extinction correction based on the UV spectral slope which may be more appropriate for 24 μm-selected sources.

We thank members of the GOODS team who contributed to the data reduction and photometric catalogs for the various data sets used here, particularly Norman Grogin, Yicheng Guo, Joshua Lee, Kyoungsoo Lee, and Harry Ferguson. We also thank G. Morrison for useful discussions. This work is based on observations made with the *Spitzer Space Telescope*, which is operated by the Jet Propulsion Laboratory, California Institute of Technology, under a contract with NASA. Support for this work was provided by NASA through an award issued by JPL/Caltech. Partly based on observations obtained with WIRCam, a joint project of Canada–France–Hawaii Telescope (CFHT), Taiwan, Korea, Canada, France, at the CFHT which is operated by the National Research Council (NRC) of Canada, the Institute National des Sciences de l'Univers of the Centre National de la Recherche Scientifique of France, and the University of Hawaii.

APPENDIX A

IR LUMINOSITY AND SFR COMPARISONS

Murphy et al. (2009) compared IR luminosities derived from 24 μm data alone to those derived when additional measurements are available, such as 16 and 70 μm photometry, submillimeter data, and mid-infrared (IRS) spectroscopy. Here, we extend this to a much larger sample of GOODS-N sources out to

Table 4
Bolometric Correction Adjustments per z Bin

Redshift					70 μm-detected		20 cm-detected	
	$L_{\rm IR}^{24}/L_{\rm IR}$	σ	$L_{\rm IR}^{24,\rm corr}/L_{\rm IR}$	σ	$L_{\rm IR}^{24}/L_{\rm IR}$	σ	$L_{\rm IR}^{\rm RC}/L_{\rm IR}$	σ
$0.0 \leqslant z < 0.4$	1.17	0.33	1.17	0.33	1.22	0.23	1.87	2.38
$0.4 \leqslant z < 0.7$	1.08	0.43	1.08	0.43	1.10	0.15	1.67	1.75
$0.7 \leqslant z < 1.0$	1.03	0.28	1.03	0.27	1.36	0.25	1.72	3.20
$1.0 \leqslant z < 1.3$	1.19	0.48	1.17	0.44	1.36	0.59	2.76	27.80
$1.3 \leqslant z < 1.9$	1.28	0.96	1.00	0.26	2.17	1.39	1.87	3.10
$1.9 \leqslant z < 2.8$	1.56	1.64	1.00	0.35	6.06	1.34	3.25	35.87

Note. Only sources having spectroscopic redshifts are considered.

$z \lesssim 3$. The redshift bins used, along with the number of sources per bin, per selection criteria, are given in Table 2. Only sources having spectroscopic redshifts are considered. Through this comparison, discrepancies between 24 μm-derived and best-fit IR luminosities are investigated. Although the 70 μm data are less sensitive than the 24 μm data, they help identify biases in the bolometric corrections at the bright end of the luminosity function.

A.1. Trends with Redshift

In Table 4, we give the median ratio of the 24 μm-derived, 24 μm-corrected, and radio-derived IR luminosities (see Appendix A.3.1) to the best-fit IR luminosities per redshift bin along with measured dispersions. The 24 μm-derived IR luminosities appear to do well by matching our best-fit IR luminosities up to redshifts of $z \lesssim 1.3$, at which point the 24 μm-derived IR luminosities appear to overestimate the true IR luminosity by $\gtrsim$30%. More interestingly, we find that the dispersion in the ratios jumps significantly once past a redshift of $z \gtrsim 1.3$, increasing by a factor of $\sim$2 and 3 in the last two redshift bins, respectively.

If we only consider those sources detected at 70 μm (i.e., the brightest sources), we find that the discrepancy between the 24 μm-derived and best-fit IR luminosities is even larger, along with the measured dispersions, once beyond $z \gtrsim 1.3$. The 24 μm-derived IR luminosity is a factor of $\sim$2 and 6 times larger than the best-fit IR luminosities in the two highest redshift bins. These discrepancies are similar to what was reported by Murphy et al. (2009), whose sample was selected to have $f_\nu(24\,\mu{\rm m}) > 200\,\mu$Jy and mid-infrared spectroscopy. This result is also consistent with that of Papovich et al. (2007) who found 24 μm-derived IR luminosities to be a factor of 2–10 times larger than those derived from stacking 70 and 160 μm data for a sample of 24 μm bright (i.e., $f_\nu(24\,\mu{\rm m}) > 250\,\mu$Jy) galaxies lying in a redshift range between $1.5 \lesssim z \lesssim 2.5$. Consequently, it appears that luminosity, and not redshift, may be the more important parameter associated with the improper SED fitting when using 24 μm photometry alone. This result agrees with what was shown in Section 3.1.2 where the residual dispersion between the ratio of the 24 μm-derived and best-fit IR luminosities was smaller when fitting versus luminosity as opposed to redshift.

In comparing the radio-derived to best-fit IR luminosities among the 20 cm-detected sources, we find that the radio (via the FIR–radio correlation) does not yield reliable IR luminosity determinations as they are $\gtrsim$2 times larger, on average, in each redshift bin. This result is likely due to the difference in the depths of the radio and *Spitzer* surveys with the radio survey being much shallower, and thus less sensitive to galaxies of the same luminosity compared with the 24 μm data (see Appendix A.3.2).

A.2. Trends with 24 μm-derived IR Luminosities

In Table 5, the same IR luminosity ratios are given as in Table 4, but per 24 μm-derived IR luminosity bin instead of redshift. For values of $L_{\rm IR}^{24} \gtrsim 10^{12.5}\,L_\odot$, the 24 μm-derived luminosity is a factor of $\sim$4 times larger than the best-fit values, on average. Not too surprisingly, when only considering those sources detected at 70 μm, we find nearly the same trend. A comparison between the radio-derived and best-fit IR luminosities among the 20 cm-detected sources shows that for all luminosity bins where $L_{\rm IR}^{24} \gtrsim 10^{10}\,L_\odot$, the radio-derived luminosities are $\sim$2 times larger than the best-fit estimates. Interestingly, we find no trend with increasing luminosity bin.

A.3. Comparison with Radio-derived SFRs: The FIR–Radio Correlation versus z

The GOODS-N field has been imaged at 1.4 GHz using the Very Large Array (VLA) for a total of 165 hr in all four configurations (Morrison et al. 2010). Since the VLA is centrally condensed, the observing time per configuration was scaled as follows, A-array (1), B-array (1/4), C-array (1/16), and D-array (1/64) (Owen & Morrison 2008). Using such an integration scaling provides the best sensitivity for extended sources. The final radio mosaic has a local rms of $\sim$3.9 μJy near the phase center covering the GOODS-N ACS area.

Taking the published GOODS-N 1.4 GHz catalog of Morrison et al. (2010), where 1230 discrete sources have been detected above a 5σ threshold, a total of 342 of lie within the ACS + 24 μm coverage. Of these sources, 286 could be matched to 24 μm detections. Among these, 194 had spectroscopic redshifts, and 192 were at $z < 3$. The 20 cm flux densities among these 192 sources span a factor of $\sim$33, ranging from $\sim$21.3 to 704 μJy. The median 20 cm flux density is $\sim$46 μJy. Sources not matched with a radio counterpart were assigned the upper limit value of 19.5 μJy.

A.3.1. Radio-derived SFRs

A nearly ubiquitous correlation is known to exist between the far-infrared (FIR; 42.5–122.5 μm) dust emission and predominantly non-thermal (e.g., 1.4 GHz) radio continuum emission arising from star-forming galaxies (de Jong et al. 1985; Helou et al. 1985). The most prominent feature of this correlation is that, at least in the local universe, it extends for galaxies spanning nearly five orders of magnitude in luminosity while exhibiting a scatter which is less than a factor of $\sim$2 (e.g., Yun et al. 2001). Massive star formation provides the common link relating these

Table 5
Bolometric Correction Adjustments per 24 μm-derived IR Luminosity Bin

Luminosity					70 μm-detected		20 cm-detected	
	$L_{\rm IR}^{24}/L_{\rm IR}$	σ	$L_{\rm IR}^{24,\rm corr}/L_{\rm IR}$	σ	$L_{\rm IR}^{24}/L_{\rm IR}$	σ	$L_{\rm IR}^{\rm RC}/L_{\rm IR}$	σ
$L_{\rm IR}^{24} < 10^{10.0}$	1.19	0.36	1.19	0.36	1.22	0.29	3.01	3.00
$10^{10.0} \leqslant L_{\rm IR}^{24} < 10^{10.5}$	1.03	0.38	1.03	0.38	1.25	0.12	1.96	3.75
$10^{10.5} \leqslant L_{\rm IR}^{24} < 10^{11.0}$	1.00	0.32	1.00	0.32	1.12	0.20	2.29	27.71
$10^{11.0} \leqslant L_{\rm IR}^{24} < 10^{11.5}$	1.13	0.42	1.13	0.42	1.10	0.12	1.88	23.22
$10^{12.0} \leqslant L_{\rm IR}^{24} < 10^{12.5}$	1.69	0.56	1.00	0.33	1.50	0.31	1.83	5.42
$L_{\rm IR}^{24} \geqslant 10^{12.5}$	3.78	1.96	1.00	0.38	3.80	1.58	2.01	3.71

Note. Only sources having spectroscopic redshifts considered.

Table 6
IR–Radio Correlation per z Bin

Redshift			70 μm-detected		20 cm-detected		20 cm +70 μm	
	$\tilde{q}_{\rm IR}$	σ_q	$\tilde{q}_{\rm IR}$	σ_q	$\tilde{q}_{\rm IR}$	σ_q	$\tilde{q}_{\rm IR}$	σ_q
$0.0 \leqslant z < 0.4$	2.26	0.39	2.62	0.28	2.41	0.27	2.44	0.19
$0.4 \leqslant z < 0.7$	2.17	0.31	2.49	0.22	2.42	0.27	2.46	0.22
$0.7 \leqslant z < 1.0$	2.07	0.36	2.47	0.16	2.41	0.26	2.43	0.12
$1.0 \leqslant z < 1.3$	2.10	0.38	2.50	0.29	2.22	0.47	2.38	0.28
$1.3 \leqslant z < 1.9$	2.07	0.29	2.43	0.16	2.37	0.31	2.43	0.18
$1.9 \leqslant z < 2.8$	2.10	0.44	2.66	0.07	2.13	0.65	2.66	0.07

Notes. Only sources having spectroscopic redshifts considered. The logarithmic IR/radio ratios and associated dispersions are given in units of dex.

two emission processes both globally and on $\lesssim$kpc scales within galaxy disks (e.g., Murphy et al. 2006, 2008; Hughes et al. 2006). Consequently, optically thin radio continuum emission is often considered to be a very good SFR diagnostic. While the FIR–radio correlation has largely been established in the local universe, there are hints that it may remain constant out to high redshifts (e.g., Garrett 2002; Appleton et al. 2004; Frayer et al. 2006; Kovács et al. 2006; Beelen et al. 2006; Vlahakis et al. 2007; Murphy et al. 2009; Murphy 2009; Sargent et al. 2010a, 2010b; Bourne et al. 2011).

We parameterize the IR–radio correlation following a similar quantitative treatment of the FIR–radio correlation (i.e., Helou et al. 1985), except that we use the total IR (8–1000 μm) luminosity, rather than the FIR fraction such that

$$q_{\rm IR} \equiv \log\left(\frac{L_{\rm IR}}{3.75 \times 10^{12} L_{\nu}(20\,{\rm cm})}\right). \quad \text{(A1)}$$

Rest-frame 1.4 GHz radio luminosities are calculated such that

$$L_{\nu}(20\,{\rm cm}) = 4\pi\, D_{\rm L}^2 S_{\nu}(20\,{\rm cm})(1+z)^{\alpha-1}, \quad \text{(A2)}$$

which includes a bandwidth compression term of $(1+z)^{-1}$ and a K-correction of $(1+z)^{\alpha}$ to rest-frame 1.4 GHz. This assumes a synchrotron power law of the form $S_{\nu} \propto \nu^{-\alpha}$ with a spectral index α for which a value of $\sim$0.8 is assumed (Condon 1992). The median $q_{\rm IR}$ value reported for a sample of 164 galaxies without signs of AGN activity is 2.64 with a dispersion of 0.26 dex (Bell 2003).

By rewriting Equation (A1), we can use the radio measurements to independently obtain estimates of the IR luminosities of each source for comparison with our template fitting. For $q = 2.64$, the radio-based IR luminosities are defined as

$$L_{\rm IR}^{\rm RC} = 1.64 \times 10^{15} L_{\nu}(20\,{\rm cm}). \quad \text{(A3)}$$

We assign a factor of $\sim$2 uncertainty to these luminosities since this is the intrinsic scatter among (e.g., Yun et al. 2001; Bell 2003) and within (e.g., Murphy et al. 2006, 2008) star-forming systems in the local universe.

A.3.2. Lack of Evolution with Redshift Out to $z \lesssim 3$

In Table 6, we give the median IR/radio ratio for each subset of sources per redshift bin given in the top of Table 2 along with the associated dispersion. By simply taking all 1107 24 μm detections with spectroscopic redshifts less than three we find median IR/radio ratios which are typically more than a factor of three lower than the locally measured value with a dispersion $\gtrsim$2 for each redshift bin. This is likely driven by the fact that only 193 (i.e., $\sim$17%) of these sources are radio detected while the remainder have IR/radio ratios calculated using the radio upper limits and are intrinsically much fainter.

Focusing on the subset of sources for which we have firm detections at 70 μm, and are most confident in the determination of their estimated IR luminosities, we find that their IR/radio ratios also show no clear signs of evolution with redshift while displaying a dispersion that is a factor of $\lesssim$2 for each redshift bin. In looking at the lowest redshift bin for these sources, we find the median IR/radio ratio and dispersion to be 2.62 and 0.28 dex, nearly identical to the average value of 2.64 dex reported by Bell (2003). At the highest redshift bin, the median $q_{\rm IR}$ value also matches that for what measured in the local universe. While the dispersion in $q_{\rm IR}$ among all 70 μm-detected sources is found to be as small as what is measured in the local universe, being $\sim$0.24 dex, we do note that the median value ($q_{\rm IR} = 2.50$ dex) is a factor of $\sim$1.37 (0.14 dex) lower than the value reported by Bell (2003). Since this departure is much smaller than the 1σ dispersion in the locally measured IR–radio correlation, and smaller in magnitude compared to the errors associated with the SED template fitting, speculating on possible physical mechanisms driving this offset is not warranted.

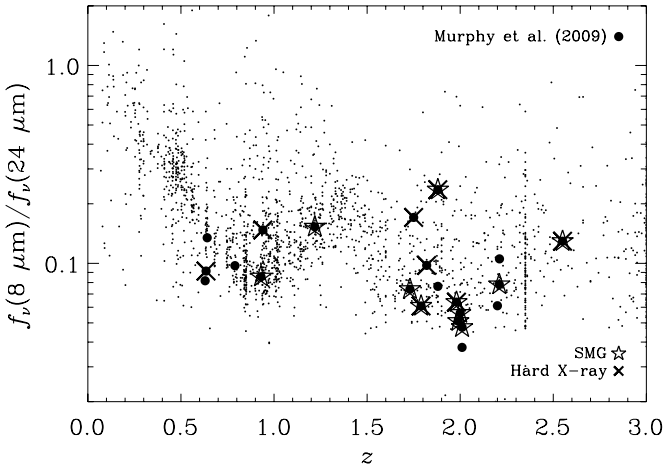

Figure 11. Ratio of 8 to 24 μm flux densities as a function of redshift for all 24 μm sources detected at 8 μm, and for which a redshift (spectroscopic or photometric) could be derived. Bold filled circles indicate the 22 galaxies included in the IRS study of Murphy et al. (2009); of these 22 galaxies, those which are SMGs and detected in the hard-band (2.0–8.0 keV) X-rays are identified by a star and cross, respectively.

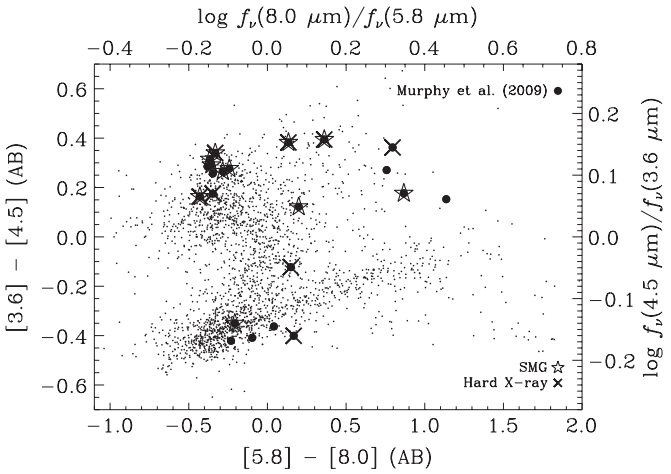

Figure 12. IRAC color–color plot for all IRAC-detected 24 μm sources usually used to identify galaxies hosting AGN (e.g., Stern et al. 2005). Bold filled circles indicate the 22 galaxies included in the IRS study of Murphy et al. (2009); of these 22 galaxies, those which are SMGs and detected in the hard-band (2.0–8.0 keV) X-rays are identified by a star and cross, respectively. The distribution of the IRS sample fills in most of the phase space covered in the IRAC color–color plot, indicating that the sample appears quite representative of galaxies spanning a range of types.

Instead, taking the IR/radio ratios for only sources having 20 cm detections, we find that the median ratios are a factor of ∼1.7–3 times lower than what is measured in the local universe. The dispersion in $q_{\rm IR}$ for these sources is also generally $\gtrsim$2 in each bin, and increasing with redshift. As with the radio-derived SFRs for all 20 cm sources, we attribute this systematic deviation in the IR/radio ratios to arise from the fact that the 20 cm detections are the brightest objects at each redshift for which the radio emission may have a considerable contribution from an AGN leading to overestimates in SFRs. Recent work by Sargent et al. (2010a) has shown that this apparent negative evolution in the FIR–radio correlation arises from comparing IR- and radio-selected samples having dramatically different sensitivity limits, with IR observations typically being much deeper than data from current radio surveys. Taking this into account, Sargent et al. (2010a) have used a survival analysis to demonstrate that the FIR–radio correlation out to similar redshift is consistent with the canonical value. Thus, we do not see any clear signatures of evolution in the FIR–radio correlation with redshift among the 70 μm-detected sources in GOODS-N, nor any significant changes in the scatter per redshift bin, although the number of sources having spectroscopic redshifts for $z \gtrsim 1.3$ is highly limited. This is not surprising since any expected evolution with redshift due to increased energy losses to cosmic-ray electrons from inverse Compton scattering off of the cosmic microwave background, resulting in depressed synchrotron emission from galaxies, should not become important until beyond $z \gtrsim 5$ (e.g., Murphy 2009; Lacki & Thompson 2010).

APPENDIX B

APPLICABILITY OF IRS SAMPLE RESULTS TO THE FULL 24 μm SAMPLE

We compare the mid-infrared photometric properties of the 22 galaxies studied by Murphy et al. (2009) to the entire 24 μm-selected sample. This is done to demonstrate that applying the bolometric and AGN corrections derived in Murphy et al. (2009) to the present sample of 24 μm sources is justified. In Figure 11, we plot the observed ratio of 8 to 24 μm flux densities versus redshift for each 24 μm source detected at 8 μm, and for which a spectroscopic or photometric redshift could be measured (i.e., 2034 of 2196 24 μm-detected sources in the ACS coverage). The 22 galaxies from Murphy et al. (2009) are shown using bold filled circles. Sources which are SMGs, and presumably star formation dominated, are identified by stars while sources which are hard X-ray-detected and likely harbor an AGN, are identified by crosses. We find that the sample of Murphy et al. (2009) spans nearly all of the 8/24 μm phase space covered by the full 24 μm-selected sample independent of the fact that the IRS sample was flux limited down to 200 μJy.

A common diagnostic tool for identifying AGN is the IRAC color–color plot (e.g., Lacy et al. 2004; Stern et al. 2005). While commonly used as a means to identify AGN, it is worth pointing out that this diagnostic does have its shortcomings. Contamination of the AGN "wedge" will occur by both low- and high-z star-forming systems, which have similar IRAC colors (e.g., Barmby et al. 2006; Donley et al. 2007; Cardamone et al. 2008). In Figure 12, we create such a plot for all IRAC-detected 24 μm sources (i.e., 2396 of 2664 24 μm-detected sources) to see if the IRS sample only occupies a single region of this phase space. We again identify the sample of Murphy et al. (2009) using bold filled circles, while SMGs and hard-band (2.0–8.0 keV) detected sources are plotted using a star and cross, respectively. It is clearly shown that the IRS sample is well distributed in IRAC color–color space, touching locations occupied by AGN and star formation dominated systems. Consequently, it appears that the IRS sample is representative of the entire 24 μm population, suggesting that applying the improved bolometric corrections and estimates for the fractional IR luminosity contributions from AGN given in Murphy et al. (2009) is warranted.

APPENDIX C

SFR COMPARISONS AMONG *BzK* SOURCES: OCCURRENCES OF IR-EXCESS SOURCES

Daddi et al. (2007a) have identified discrepancies between the UV, radio, and IR derived SFR estimates in $z \sim 2$ galaxies

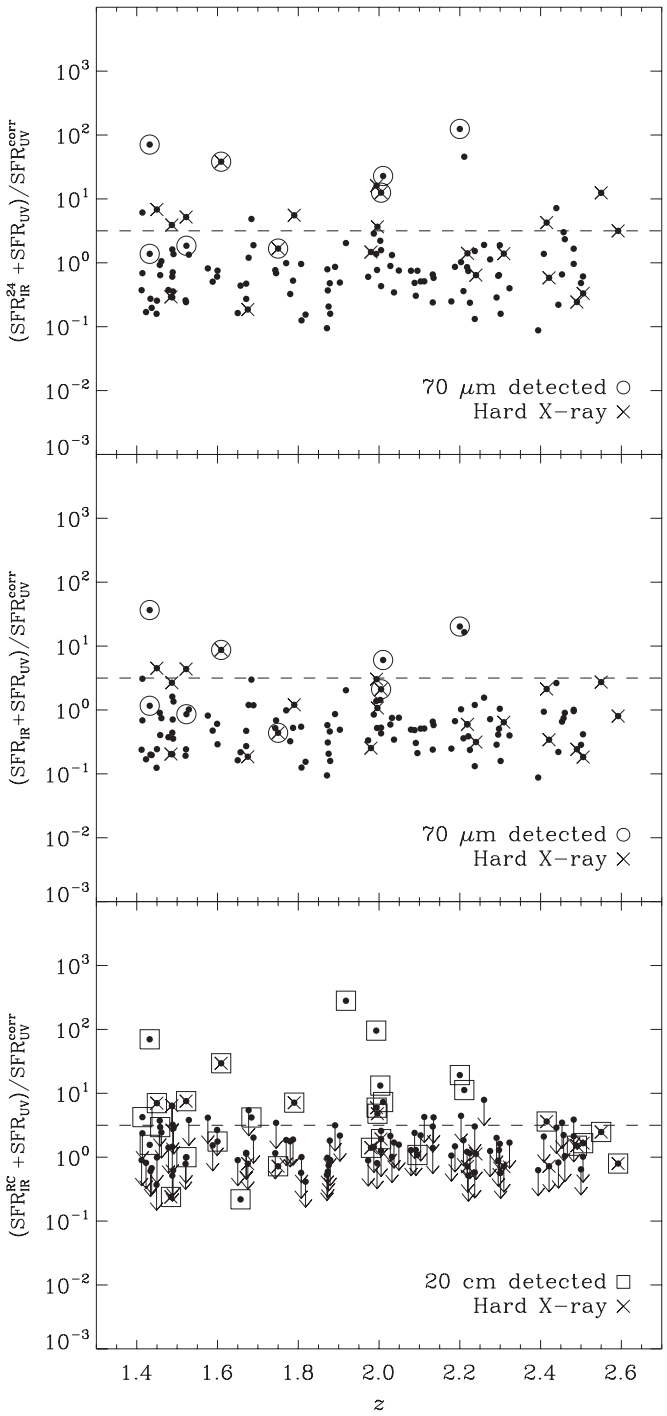

Figure 13. We plot the ratio of IR-based SFR estimates (plus the observed UV-derived SFR) to extinction-corrected UV SFRs as a function of redshift between $1.4 < z < 2.6$ for sources which we were able to measure rest-frame 1500 Å flux densities. In the top panel, the IR-based SFR was calculated using IR luminosity estimates by SED fitting the 24 μm flux densities alone while the middle panel uses the best-fit IR luminosities to calculate the IR-based SFRs. In the bottom panel, we use the 20 cm radio continuum flux densities and the FIR–radio correlation to derive the SFRs (SFR_{IR}^{RC}). The SFRs are considered to be upper limits for those galaxies not detected at 20 cm (downward arrows). In each panel, the dashed line indicates where the logarithm of this ratios is equal to 0.5 dex; galaxies having values higher than this are considered to be IR-excess sources (Daddi et al. 2007a). Galaxies detected at 70 μm are identified with open circles while those that are detected in hard-band (2.0–8.0 keV) X-rays are indicated by a cross.

selected using the *BzK* selection technique. Following the criterion of Daddi et al. (2007a, 2007b), we calculate whether

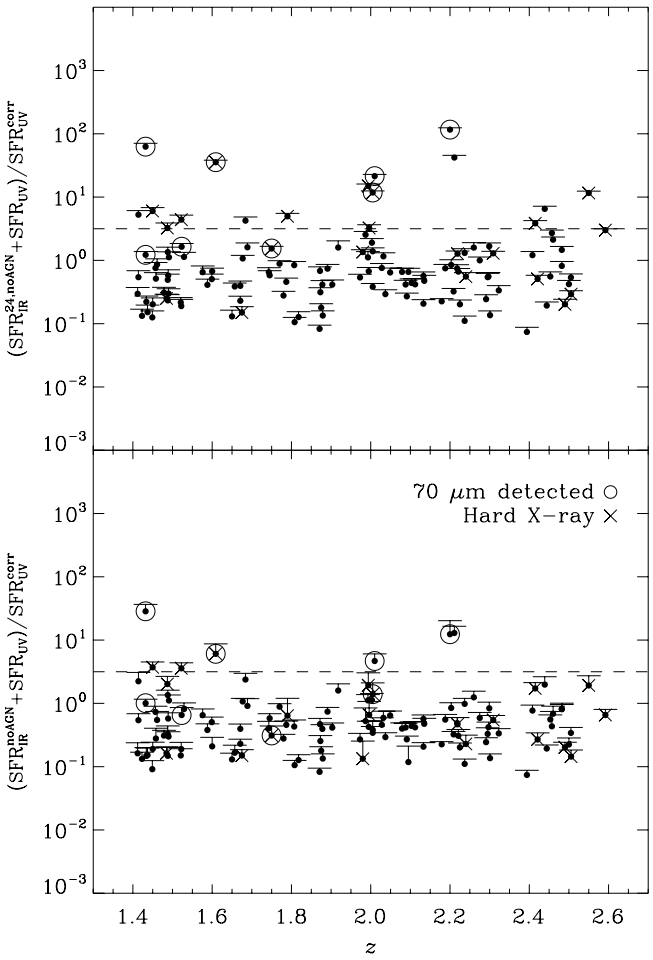

Figure 14. Same as the top two panels in Figure 11 except that we correct the 24 μm and best-fit IR luminosities for the contribution from AGN. The decrease is shown by a vertical line attached to a short horizontal line, and is 20%, on average, in both panels. The AGN luminosity used to correct the IR-based SFR was determined using the relation derived in Murphy et al. (2009) between the AGN contribution to the IR luminosity and the difference between best-fit IR luminosities and those derived from 24 μm photometry alone (see Section 3.1.3). Sources that are detected in the hard-band (2.0–8.0 keV) X-rays are identified by crosses.

galaxies have a mid-infrared excess by measuring the ratio of IR + (observed) UV SFRs to that of the extinction-corrected UV SFR. Sources having

$$\log\left(\frac{\mathrm{SFR_{IR}} + \mathrm{SFR_{UV}}}{\mathrm{SFR_{UV}^{corr}}}\right) > 0.5 \qquad \text{(C1)}$$

are considered to be "mid-infrared excess" sources. We note that while the numerator contains a term for the UV emission which may escape the galaxy before being absorbed and re-radiated in the infrared by dust, this term is often negligible compared to the IR-based SFR term.

Using the 24 μm-derived, radio-derived, and best-fit estimates for IR luminosity to derive SFRs, we plot the ratio of IR+UV to UV-corrected SFRs for sources having spectroscopic redshifts in the range between $1.4 < z < 2.6$ detected at 24 μm for which we were also able to estimate a rest-frame 1500 Å flux density. The IR-based SFRs in the top panel of Figure 11 are calculated using the 24 μm-derived IR luminosities, the middle panel uses our best-fit IR luminosities, and the bottom panel uses IR-based SFRs estimated using the radio continuum imaging and the FIR–radio correlation.

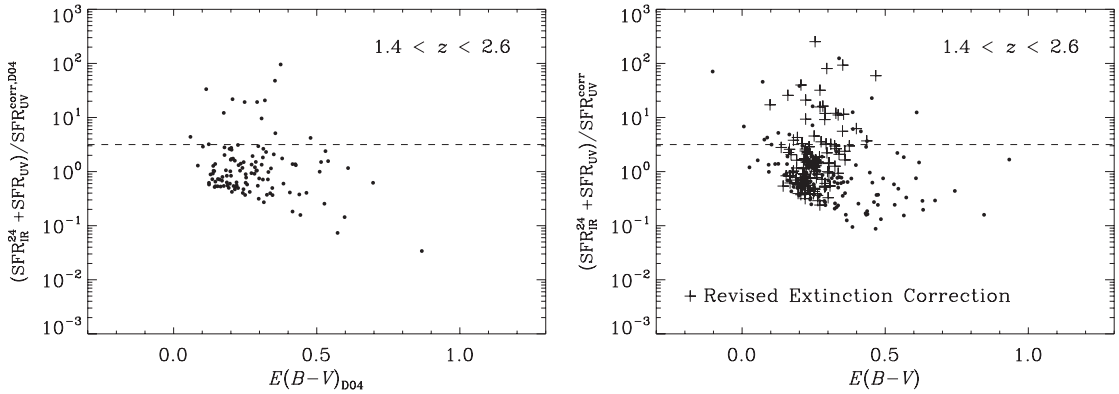

Figure 15. Ratio of IR-derived SFRs estimated from SED fitting (plus UV-derived SFRs uncorrected for extinction) to extinction-corrected UV SFRs against the color excess $E(B-V)$ inferred from fitting the rest-frame UV (1250–2600 Å) slope using *UBViz* optical imaging data for only those spectroscopically detected galaxies lying within a redshift range between $1.4 < z < 2.6$ (i.e., approximately the *BzK* selection range). This is done to illustrate the difference in extinctions derived by using color relations (left panel; i.e., Daddi et al. 2004) to that when a proper slope is fit (right panel). The plus symbols in the right panel were generated using our revised extinction corrections (see Section 4).

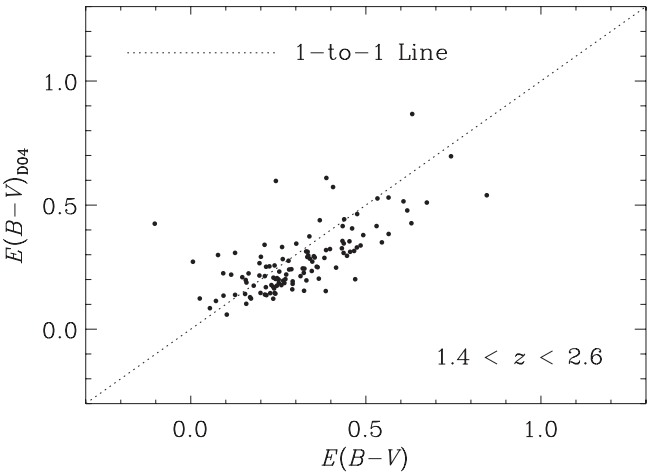

Figure 16. Comparison of extinction estimates for galaxies lying within a redshift range between $1.4 < z < 2.6$ (i.e., approximately the *BzK* selection range). Extinctions calculated using color relations from Daddi et al. (2004) are plotted against estimates from directly fitting the UV slope (see Figure 13). A one-to-one line is plotted as a dotted line. The direct fitting methods tend to yield larger reddening values.

Excluding the hard-band (2.0–8.0 keV) X-ray-detected sources, for which AGNs are likely present, we find that the number of sources lying above the mid-infrared excess criterion decreases dramatically (i.e., from 7 to 4, a factor of ∼2) by using the best-fit IR luminosities rather than those derived using the 24 μm photometry alone. This is consistent with the findings of Murphy et al. (2009) who reported that ≈50% of their "mid-infrared excess" sources could be accounted for by better constrained bolometric corrections rather than the subtraction of emission from obscured AGN which was estimated using deep mid-infrared spectroscopy. Instead, looking at the radio-derived IR luminosities for those sources detected at 20 cm, we find that the number of mid-infrared excess sources is actually larger than when using the 24 μm-derived IR luminosities, being 9 and 6, respectively.

C.1. Corrections for AGN

While the improved bolometric correction was able to account for ≈50% mid-infrared excess sources (Figure 13), we find that by subtracting our estimates for the AGN contribution to the IR luminosities, all galaxies remain mid-infrared excess sources (top panel of Figure 14). The AGN contribution is indicated by the distance between the horizontal line and solid points. This finding is consistent with Murphy et al. (2009) who reported that the existence of the mid-infrared excess sources was dominated by an overestimate in the bolometric corrections rather than embedded AGN. This is contrary to the suggestion inferred by Daddi et al. (2007a), whose conclusion was based on the presence of a hard X-ray source through X-ray stacking. Accordingly, our result suggests that the sky and space densities of Compton-thick AGN reported by Daddi et al. (2007b) are high by a factor of ∼2, and are likely more consistent with values of ∼1600 deg^{-2} and ∼1.3×10^{-4} Mpc^{-3}, respectively.

In the bottom panel of Figure 14, we plot the ratio of AGN-corrected IR (plus the observed UV) SFRs to extinction-corrected UV SFRs and find the same occurrence of mid-infrared excess sources (four sources, three of which are 70 μm-detected), again suggesting that AGNs are not causing the discrepancy between the IR and UV SFRs; among all the galaxies plotted, the application of Equation (3) suggests that AGNs only contribute $\lesssim$25% of their total IR luminosity, on average. To explain the galaxies which persist as mid-infrared excess sources, Murphy et al. (2009) suggested that it may have to due with improper extinction corrections relying on the slope of the UV continuum such that the extinctions for these sources are underestimated, thereby yielding underestimates for the UV-derived SFRs. In this scenario, the extinction within a galaxy is so high that the interstellar medium (ISM) becomes optically thick, causing the relation between extinction and the slope of UV continuum to fail.

C.2. UV Extinction Corrections

To compare how well simple color relations work to estimate extinction versus actually fitting the UV slopes of each objects, we plot the ratio of IR + UV to UV-corrected SFRs in the in Figure 15 against $E(B-V)$ color excesses calculated using the color relation given by Daddi et al. (2004, $E(B-V)_{\rm D04} = 0.25(B-z+0.1)_{\rm AB}$; left panel) and from a proper fit to the rest-frame UV continuum (right panel). The UV-corrected SFRs used in the ratios were calculated using the respective methods to compute the extinction corrections. Figure 16 also compares the color excess $E(B-V)$ derived by the two methods. The direct fitting method tends to yield larger reddening values, particularly for objects with redder UV spectral slopes. The median $E(B-V)$ changes from ∼0.25 to 0.29 mag between

the color-fitting *BzK* method of Daddi et al. (2004) and the direct fits to the UV slope for individual galaxies as defined here. The median UV extinction correspondingly changes from ∼2.0 to 2.4 mag, corresponding to an increase in the median UV-derived SFR by a factor of ∼1.5. Comparison of the two methods as a function of redshift shows that the dispersion between them increases at the extremes of the redshift range for *BzK* selection (i.e., near $z = 1.4$ and 2.6). For comparison, the sources in the right panel of Figure 15 are re-plotted using the revised extinction corrections (i.e., Equation (5)) as plus symbols. Accordingly, using this color relation, rather than directly fitting the UV continuum for computing extinction corrections in this redshift range, does appear to introduce a systematic uncertainty for computing the UV-corrected SFRs.

REFERENCES

Alexander, D. M., et al. 2003, AJ, 126, 539
Appleton, P. N., et al. 2004, ApJS, 154, 147
Armus, L., et al. 2007, ApJ, 656, 148
Barger, A. J., Cowie, L. L., & Wang, W.-H. 2008, ApJ, 689, 687
Barmby, P., et al. 2006, ApJ, 642, 126
Beelen, A., Cox, P., Benford, D. J., Dowell, C. D., Kovács, A., Bertoldi, F., Omont, A., & Carilli, C. L. 2006, ApJ, 642, 694
Bell, E. F. 2002, ApJ, 577, 150
Bell, E. F. 2003, ApJ, 586, 794
Berta, S., et al. 2010, A&A, 518, L30
Bourne, N., Dunne, L., Ivison, R. J., Maddox, S. J., Dickinson, M., & Frayer, D. T. 2011, MNRAS, 410, 1155
Bruzual, A. G. 2007, in IAU Symp. 241, Stellar Populations as Building Blocks of Galaxies, ed. A. Vazdekis & R. F. Peletier (Cambridge: Cambridge Univ. Press), 125
Bruzual, G., & Charlot, S. 2003, MNRAS, 344, 1000
Buat, V., et al. 2005, ApJ, 619, L51
Buat, V., et al. 2010, MNRAS, 409, L1
Capak, P., et al. 2004, AJ, 127, 180
Caputi, K. I., et al. 2007, ApJ, 660, 97
Cardamone, C. N., et al. 2008, ApJ, 680, 130
Chary, R.-R. 2007, in ASP Conf. Ser. 380, At the Edge of the Universe, ed. J. Afonso, H. Ferguson, & R. Norris (San Francisco, CA: ASP), 375
Chary, R.-R., & Elbaz, D. 2001, ApJ, 556, 562
Cohen, J. G., Hogg, D. W., Blandford, R., Cowie, L. L., Hu, E., Songaila, A., Shopbell, P., & Richberg, K. 2000, ApJ, 538, 29
Condon, J. J. 1992, ARA&A, 30, 575
Daddi, E., Cimatti, A., Renzini, A., Fontana, A., Mignoli, M., Pozzetti, L., Tozzi, P., & Zamorani, G. 2004, ApJ, 617, 746
Daddi, E., et al. 2007a, ApJ, 670, 156
Daddi, E., et al. 2007b, ApJ, 670, 173
Dale, D. A., & Helou, G. 2002, ApJ, 576, 159
Dale, D. A., Helou, G., Contursi, A., Silbermann, N. A., & Kolhatkar, S. 2001, ApJ, 549, 215
Dale, D. A., et al. 2005, ApJ, 633, 857
de Jong, T., Klein, U., Wielebinski, R., & Wunderlich, E. 1985, A&A, 147, L6
Dickinson, M., Giavalisco, M., & GOODS Team 2003, in The Mass of Galaxies at Low and High Redshift, ed. R. Bender & A. Renzini (Berlin: Springer), 324
Dole, H., et al. 2006, A&A, 451, 417
Donley, J. L., Rieke, G. H., Pérez-González, P. G., Rigby, J. R., & Alonso-Herrero, A. 2007, ApJ, 660, 167
Downes, D., & Solomon, P. M. 1998, ApJ, 507, 615
Draine, B. T. 2003, ARA&A, 41, 241
Dye, S., Eales, S. A., Ashby, M., Huang, J.-S., Egami, E., Brodwin, M., Lilly, S., & Webb, T. 2007, MNRAS, 375, 725
Elbaz, D., Cesarsky, C. J., Chanial, P., Aussel, H., Franceschini, A., Fadda, D., & Chary, R. R. 2002, A&A, 384, 848
Elbaz, D., et al. 2010, A&A, 518, L29
Engelbracht, C. W., et al. 2006, ApJ, 642, L127
Farrah, D., Afonso, J., Efstathiou, A., Rowan-Robinson, M., Fox, M., & Clements, D. 2003, MNRAS, 343, 585
Fischer, J., et al. 2010, A&A, 518, L41
Frayer, D. T., et al. 2006, ApJ, 647, L9
Frayer, D. T., et al. 2009, AJ, 138, 1261
Garrett, M. A. 2002, A&A, 384, L19
Giavalisco, M., et al. 2004, ApJ, 600, L93
Gonzalez, A. H., Clowe, D., Bradač, M., Zaritsky, D., Jones, C., & Markevitch, M. 2009, ApJ, 691, 525
Helou, G., Soifer, B. T., & Rowan-Robinson, M. 1985, ApJ, 298, L7
Houck, J. R., et al. 2004, ApJS, 154, 18
Hughes, A., Wong, T., Ekers, R., Staveley-Smith, L., Filipovic, M., Maddison, S., Fukui, Y., & Mizuno, N. 2006, MNRAS, 370, 363
Kennicutt, R. C., Jr. 1998, ARA&A, 36, 189
Kong, X., Charlot, S., Brinchmann, J., & Fall, S. M. 2004, MNRAS, 349, 769
Kovács, A., Chapman, S. C., Dowell, C. D., Blain, A. W., Ivison, R. J., Smail, I., & Phillips, T. G. 2006, ApJ, 650, 592
Lacki, B. C., & Thompson, T. A. 2010, ApJ, 717, 196
Lacy, M., et al. 2004, ApJS, 154, 166
Lagache, G., Dole, H., & Puget, J.-L. 2003, MNRAS, 338, 555
Laird, E. S., Nandra, K., Adelberger, K. L., Steidel, C. C., & Reddy, N. A. 2005, MNRAS, 359, 47
Le Borgne, D., & Rocca-Volmerange, B. 2002, A&A, 386, 446
Le Floc'h, E., et al. 2005, ApJ, 632, 169
Madden, S. C., Galliano, F., Jones, A. P., & Sauvage, M. 2006, A&A, 446, 877
Magdis, G. E., Elbaz, D., Daddi, E., Morrison, G. E., Dickinson, M., Rigopoulou, D., Gobat, R., & Hwang, H. S. 2010, ApJ, 714, 1740
Magnelli, B., Elbaz, D., Chary, R. R., Dickinson, M., Le Borgne, D., Frayer, D. T., & Willmer, C. N. A. 2009, A&A, 496, 57
Magnelli, B., Elbaz, D., Chary, R. R., Dickinson, M., Le Borgne, D., Frayer, D. T., & Willmer, C. N. A. 2011, A&A, 528, A35
McLure, R. J., Jarvis, M. J., Targett, T. A., Dunlop, J. S., & Best, P. N. 2006, MNRAS, 368, 1395
Meurer, G. R., Heckman, T. M., & Calzetti, D. 1999, ApJ, 521, 64
Morrison, G., et al. 2010, ApJS, 188, 178
Murphy, E. J. 2009, ApJ, 706, 482
Murphy, E. J., Chary, R.-R., Alexander, D. M., Dickinson, M., Magnelli, B., Morrison, G., Pope, A., & Teplitz, H. I. 2009, ApJ, 698, 1380
Murphy, E. J., Helou, G., Kenney, J. D. P., Armus, L., & Braun, R. 2008, ApJ, 678, 828
Murphy, E. J., et al. 2006, ApJ, 638, 157
Nordon, R., et al. 2010, A&A, 518, L24
Owen, F., & Morrison, G. 2008, AJ, 136, 1889
Papovich, C., et al. 2007, ApJ, 668, 45
Pérez-González, P. G., et al. 2005, ApJ, 630, 82
Pope, A., et al. 2008, ApJ, 675, 1171
Reddy, N. A., Erb, D. K., Pettini, M., Steidel, C. C., & Shapley, A. E. 2010, ApJ, 712, 1070
Reddy, N. A., Erb, D. K., Steidel, C. C., Shapley, A. E., Adelberger, K. L., & Pettini, M. 2005, ApJ, 633, 748
Reddy, N. A., Steidel, C. C., Fadda, D., Yan, L., Pettini, M., Shapley, A. E., Erb, D. K., & Adelberger, K. L. 2006, ApJ, 644, 792
Reddy, N. A., Steidel, C. C., Pettini, M., Adelberger, K. L., Shapley, A. E., Erb, D. K., & Dickinson, M. 2008, ApJS, 175, 48
Rieke, G. H., et al. 2004, ApJS, 154, 25
Rigby, J. R., et al. 2008, ApJ, 675, 262
Rodighiero, G., et al. 2010, A&A, 515, A8
Sajina, A., Yan, L., Armus, L., Choi, P., Fadda, D., Helou, G., & Spoon, H. 2007, ApJ, 664, 713
Salpeter, E. E. 1955, ApJ, 121, 161
Sanders, D. B., Mazzarella, J. M., Kim, D.-C., Surace, J. A., & Soifer, B. T. 2003, AJ, 126, 1607
Sargent, M. T., et al. 2010a, ApJS, 186, 341
Sargent, M. T., et al. 2010b, ApJ, 714, L190
Siana, B., Teplitz, H. I., Chary, R.-R., Colbert, J., & Frayer, D. T. 2008, ApJ, 689, 59
Smith, J. D. T., et al. 2007, ApJ, 656, 770
Stern, D., et al. 2005, ApJ, 631, 163
Teplitz, H. I., Charmandaris, V., Chary, R., Colbert, J. W., Armus, L., & Weedman, D. 2005, ApJ, 634, 128
Teplitz, H. I., et al. 2011, AJ, 141, 1
Veilleux, S., et al. 2009, ApJS, 182, 628
Vlahakis, C., Eales, S., & Dunne, L. 2007, MNRAS, 379, 1042
Wang, W.-H., Cowie, L. L., Barger, A. J., Keenan, R. C., & Ting, H.-C. 2010, ApJS, 187, 251
Weingartner, J. C., & Draine, B. T. 2001, ApJ, 548, 296
Wilson, G. W., et al. 2008, MNRAS, 390, 1061
Wirth, G. D., et al. 2004, AJ, 127, 3121
Xu, C., Lonsdale, C. J., Shupe, D. L., O'Linger, J., & Masci, F. 2001, ApJ, 562, 179
Yun, M. S., Reddy, N. A., & Condon, J. J. 2001, ApJ, 554, 803